Dear Editor,

We are submitting the revised version of our manuscript for consideration for publication in Biogeosciences.

All comments of the reviewers have been addressed in this revised version of our manuscript. In particular to address the model resolution comment of reviewer #2, we have performed all simulations again in the higher horizontal resolution of our model. The figures have been appropriately redrawn; tables and text have been accordingly updated. The conclusions of the paper remain unchanged since the discussion paper. Discussion has been improved to highlight also the importance of primary dissolved Fe emissions in the computed atmospheric deposition changes. We have also added comments on uncertainties and performed small linguistic corrections.

We would like to thank both anonymous reviewers of our manuscript for the careful reading and the useful comments that helped improving our manuscript. We provide here-below our point-by-point replies to the comments of the reviewers.

We thank you very much for your time and we hope that this revised version is suitable for publication in Biogeosciences.

<u>Point-by-point reply to the comments of the Reviewer #1</u>

1) *p. 3945, l.9: What do you mean by "up to" 50%?*

- For clarity, the sentence in the abstract has been rephrased as follows: 'Proton- and organic ligand-promoted Fe-dissolution in present-day TM4-ECPL simulations is calculated to be ~0.175 Tg-Fe yr^{-1}, approximately half of the calculated total primary DFe emissions from mineral and combustion sources in the model (~0.322 Tg-Fe yr^{-1}) (line 32 in the revised manuscript).

2) p. 3947, l19: *3% should be replaced with 5% of hematite in dust.*

- The typo has been corrected (line 157 in the revised manuscript).

3) *p.3948, l.17: inorganic should be replaced with inorganic acids. Please delete ammonium.*

- Corrected (lines 201-202 in the revised manuscript).

3) *p.3948, l.26: More recent study developed an explicit scheme for iron dissolution of combustion aerosols due to photochemical reactions with inorganic and organic acids in solution (Ito, 2015).*

- This manuscript has been submitted prior the publication of Ito (2015). We now make reference to that study as follows: "*A recent modelling study by Ito (2015), published after the submission of the present work, focusing on the atmospheric processing of Fe-containing combustion aerosols by photochemical reactions with inorganic and organic acids indicates that ligand (OXL)-promoted Fe dissolution more than doubles the calculated DFe deposition from combustion sources over certain regions of the global ocean."* (lines 217-232 in the revised manuscript).

4) *p. 3949, l.3: Please correct the reference of Mahowald et al. (2009) to Luo et al (2008) & p. 3949, l.10: The sentence for the same study is repeated. Please correct or delete it*

- We have rephrased this part to avoid repetition and to point to the original study by Luo et al (2008) as:
  "*Mineral-Fe represents ~95% of the global atmospheric TFe source, with combustion Fe sources responsible for the remaining ~5% (Luo et al., 2008; Mahowald et al., 2009). Luo et al. (2008) accounted for both soluble and*

insoluble forms of Fe emissions from biomass burning and anthropogenic combustion processes in relation to Black Carbon (BC) emissions and they estimated (based on observed Fe/BC ratios) that ~1.7 Tg-Fe·yr^{-1} are emitted to the atmosphere via combustion processes. Mahowald et al. (2009) also indicates that humans may significantly impact DFe deposition over oceans by increasing both the acidity of atmospheric aerosol, as well as the DFe emissions from combustion processes." (lines 235-245 in the revised manuscript).

5) *p.3951, l. 13: How did you calculate the dust emissions of 1090 Tg/yr for the year 2008 from the AEROCOM emission of 1678 Tg/yr for the year 2000?*

- Dust emission fields are specific for the year 2008 and provided by E. Vignati. They have been prepared using an application of the Tegen model (Tegen et al., JGR 107, D21, 2002), extended by B. Heinhold (JGR, 112, 2007) and adapted by E. Vignati using the ECMWF fields as input to be coherent with the TM4/TM5 input.

6) *p.3951, l. 19: How did you calculate the emissions for the year 2008 from the ACCMIP database for the year 2000?*

ACCMIP emissions for the year 2008 are available on-line through the ECCAD database (http://eccad.sedoo.fr/eccad_extract_interface/JSF/page_meta.jsf). Appropriate information has been added in the revised manuscript in section 2.1 (line 321 in the revised manuscript).

7) *p 3952, l3: How did you apply the 1°×1° dataset to the dust emission in the 6°×4° model?*

- All inputs to the model are in 1°x1° resolution. The mineralogy datasets were first re-gridded (average) from the original 30s resolution to the 1◦ × 1◦ grid resolution and then applied to the daily dust emissions used by the model. Then the model re-grids the fields (sum or average) to the desired resolution. To clarify this, we added the following sentences in the manuscript:
  "In the present study, the global soil mineralogy dataset developed by Nickovic et al. (2012) at 30" resolution (~1 km) has been initially re-gridded to 1°x1° global resolution and applied to the 1°x1° daily dust emissions taken into account by TM4-ECPL." (line 350-352 in the revised manuscript).

8) *p.3954, l.16: It reads that the pH values do not depend on aerosol sizes and types. Do you assume the internal mixing of all the aerosols in calculating aerosol water pH? What is the definition of aerosol water pH in your model?*

> Aerosol pH values do depend on aerosol size and types. We add the following test in the manuscript: *"Aerosol pH and water are here calculated for each aerosol mode (Fig. S2a for the fine mode and Fig. S2b for the coarse mode). The pH values for each aerosol mode are calculated by the thermodynamic equilibrium model ISORROPIA II assuming internal mixing of the aerosols (Fountoukis and Nenes, 2007). Briefly, for each mode (fine and coarse) sulphate, nitrate, ammonium and sea-salt (i.e. K^+; Ca^{2+}; Mg^{2+}; Na^+; SO_4^{2-}; Cl^-) aerosols are assumed to be internally mixed. Carbonates ($CaCO_3$, $MgCO_3$) and gypsum ($CaSO_4$) are considered to be present in the silt soil particles (Meskhidze et al., 2005), with their impact on the coarse particulate H^+ and H_2O, to be calculated interactively by the ISORROPIA II. The dissolved Ca^{+2} and Mg^{+2} is distributed by the thermodynamic model among all possible solids."* (line 466-475 in the revised manuscript).

9) *p. 3954, l.21: Why did you use the mean percent mass content of particles for dust, instead of the mineralogy map? How did you consider the dissolution (e.g., calcite and magnetite) and precipitation (e.g., gypsum) for these minerals?*

- The mean percent content had been used to limit the computing time. We have now repeated the simulations using the mineralogy map for the fraction of Ca^{+2} on dust by Nickovic et al. (2012). However, since that database does not provide mineralogy map for magnesite, the 5.5% fraction on dust as mentioned in Ito and Feng (2010) is used as in the discussion paper. The following sentence has been added in the text:
  "The global soil mineralogy dataset (Nickovic et al., 2012) has been applied on dust emissions to calculate the concentrations of Ca^{+2} on dust particles (calcite ($CaCO_3$) and gypsum ($CaSO_4$))." (lines 453-464 in the revised manuscript).

- The dissolution and precipitation of Mg^{+2} and Ca^{+2} (carbonates and gypsum) are calculated by the thermodynamic equilibrium model. ISORROPIA II takes into account the sum of the aforementioned crustal species and based on thermodynamic equilibrium distributes them to various salts e.g. $CaCO_3$, $CaSO_4$, $Ca(NO_3)_2$, $CaCl_2$ etc. Moreover, ISORROPIA II assumes $MgSO_4(s)$ to be always deliquesced when an aqueous phase is present as well as that $CaSO_4$ is completely insoluble.

10) p. *3955, l.3, Table 2: The values of KMIN for KAOLINITE and FELDSPARS are different from those in the reference, but are identical to that for HEMATITE. Please check the values.*

- We thank the reviewer for pointing these typos in the Table. It is now corrected. (line 1756 in the revised manuscript).

11) *p. 3956, l.5: How did you set the cloud life time?*

TM4-ECPL is an offline CTM and does not explicitly calculate clouds and precipitation. These are input to the model taken from the ERA-interim ECMWF dataset.

12) *p.3956, l.19: The reaction rate for OXL-promoted Fe dissolution was determined in cloud water conditions, so that this was only applied to cloud droplets. I agree that this oxalate-promoted dissolution should not be applied to mineral aerosols under these low pH conditions (see below). However, if you want to argue that "under these low pH conditions, ligand-promoted Fe dissolution may be suppressed significantly", please show the results. It is more likely that ligand-promoted Fe dissolution is suppressed "under low oxalate concentration" (Ito, 2015), because of no significant oxalic acid sources near the desert regions, as you also mentioned in this manuscript.*

- According to the Fe-dissolution scheme used in the present study, OXL (i.e. $(COO^-)_2$) and not the total oxalic acid (i.e. TOXL = $(COOH)_2$ + $HOOC\text{-}COO^-$ + $(COO^-)_2$) is considered to promote the Fe-dissolution (as also in the Johnson and Meskidze, 2013). Oxalic acid has pKa1 = 1.27 and pKa2 = 4.27 and since the mole fraction of $(COO^-)_2$ is suppressed significantly in acidic environments, the OXL-promoted Fe-dissolution is expected also to be suppressed. This is discussed in section 2.6, second paragraph and supported by the shown box model calculations.
- However, we agree with the reviewer that this sentence at the end of section 2.4.2 might be confusing thus it has been rephrased as:
- *"Thus, under such conditions of low aqueous-phase OXL concentrations, the ligand-promoted Fe dissolution may be suppressed significantly"* (lines 549-550 in the revised manuscript).

13) *Lin et al. (2014) showed that the model with iron chemistry underestimated oxalate measurements. Please show the comparison of oxalate measurements with iron chemistry, as in Fig 6 (b) of Myriokefalitakis et al. (2011).*

- Indeed in our calculation, as well, Fe-chemistry suppresses OXL atmospheric production through the aqueous-phase Fe-oxalato complexes photo-dissociation to CO_2 via: $[Fe(C_2O_4)_2]^- + h\nu + (+ O_2) \rightarrow Fe^{2+} + C_2O_4^{2-} + 2CO_2 + O_2^-$
  The requested figure is now added in Fig. S3 in the supplement.

14) *Figure S9: This figure was requested in review of Johnson and Meskhidze (2013), but was not shown (Interactive comment on Geosci. Model Dev. Discuss., 6, 1901, 2013). It is extremely hard to accept higher iron solubility (10%) for mineral dust with oxalate at pH = 8.5 than that at pH = 1.5 after 10 days in reality. Laboratory studies for dust aerosols showed that dissolved Fe with oxalate is higher at lower pH (see Figure S2 in Chen and Grassian, 2013). This is mainly because the oxalate-promoted dissolution rate of minerals is dependent on the mineral surface concentration of oxalate. Please show the spatial distribution of SFe (%) for dust aerosols and pH in water (see below).*

- In the discussion paper we have performed 10 days dissolution 'box-model' simulations considering both pH and OXL concentrations constant in order to estimate the relative contribution of protons and oxalate concentrations (i.e. an Open System (see Seinfeld and Pandis, 2006, p. 318) where OXL and pH are maintained at constant values; presumably by continuous infusion of new OXL and acidic compounds (however not realistic)).
- In order to avoid any confusion we performed new simulations with pH values constant but with oxalate concentrations allowed to change during the simulation time. Initial oxalic acid concentrations are provided and oxalate is calculated by considering the transformation of oxalic acid among $(COOH)_2$, $HOOC\text{-}COO^-$, $(COO^-)_2$ and Ferrus/Ferric-Oxalato complexes in the aqueous phase as well as losses by photodissociation to CO_2 as shown in Table S2. These results are shown in the new figure S4 (lines 584-679 in the revised manuscript).
- To satisfy the reviewer, we have now calculated separately the spatial distribution of SFe for mineral dust, as well as for fossil fuel and for biomass burning aerosol. These are now shown in the supplementary figures S6b,c,d respectively together with the total SFe in Figure S6a. The spatial distributions of pH in aerosol water and in clouds are shown as requested in the supplementary figures S2a-d.

15) *Did you use daily or monthly or annual mean concentration for the comparison with the daily measurements? Please clarify this. Could you show the comparison of iron solubility?*

- For comparison with the data compiled by Sholkovitz et al. (2013) for the Atlantic Ocean (Baker et al., 2013) and the Indian Ocean (Witt et al., 2006) we use daily mean model concentrations. We rephrased the text appropriately *"TM4-ECPL daily mean results are here validated against daily observations of total (Fig. 5a) and dissolved Fe (Fig. 5b) associated with atmospheric aerosols over the Atlantic Ocean (Baker et al., 2013) and the Indian Ocean (Witt et al., 2006) as compiled by Sholkovitz et al. (2013)."* (line 879 in the revised manuscript).

- Iron solubility calculated by the model with observations are now also depicted in Fig. 5. *"Figure 5c also presents the comparison of daily solubility fractions of the above observations versus the respective calculated fractions by the model."*

16) *Please show the spatial distribution of iron solubility for mineral dust. Could you also show the spatial distribution of iron solubility for the fast-released iron, intermediate released iron, and slowly-released iron, respectively, in supplementary materials?*

- The spatial distribution of %SFe for dust aerosol has been added in the supplementary figures S6a (see comment 14).
- Although we use separate species for each type of mineral-released Fe, for computational efficiency reasons, we do not track the dissolved Fe from each mineral pool, so we cannot produce a figure for the spatial distribution of iron solubility for each iron type.

17) *Could you show the comparison of iron solubility?*

- This has been added (Figure 5c).

18) *Figure S4: Could you show the distributions of aerosol pH and cloud pH?*

- Mean pH values of surface aerosol and cloud at 850hPa are added in the supplement (figure S2) (see comment 14)

19*) p. 3965, l.27: How did you separate the proton Fe dissolution from ligand Fe dissolution? Please discuss iron speciation quantitatively, by showing figure or table.*

- Proton- and ligand- dissolution are separated processes in our model. Since each type of dissolution is a kinetic process – it is parameterised like a separate chemical reaction and its reaction budget can be derived from the model output.
- Iron speciation is based on the chemical scheme used for this study. Fig. S5, shows the spatial distribution of Fe(III) - sum of Fe^{3+} and Ferric-Oxalato complexes, and Fe(II) - sum of Fe^{2+} and Ferrus-Oxalato complexes and Fe(II)

20) *p. 3966, l.6: Please show the comparison of iron speciation with the observation quantitatively. Figure 4c shows the ratio is less than 10% over the significant portions of the ocean. If the modeled ratio is higher in rainwater, please show the results.*

- The observations we dispose in our database (see answer 15) do not provide systematic information on the Fe speciation. The few existing deposition data (Theodosi et al., 2010) show higher Fe(II) contribution in DFe that simulated by our model. This is now discussed in the revised manuscript in the last paragraph of section 4.1 *"our model calculates much lower Fe(II) content in DFe (Fig. 4c) compared to that study indicating a model underestimate of Fe(II) source potentially those associated with the organic ligand promoted contribution to DFe."* (lines 1118-1120 in the revised manuscript).

  The figures provided herebelow show that the modelled Fe(II)/DFe ratio in wet deposition (a) follows the distribution of the surface Fe(II)/DFe concentration ratio (b). The model calculates high fractions of Fe(II)/DFe deposition fluxes over the equatorial Pacific due to large scale precipitation and to relatively enhanced Fe(II) concentrations as also seen in the Fe(II)/DFe surface concentrations fraction.

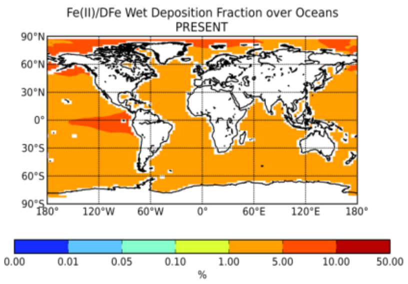

(a)

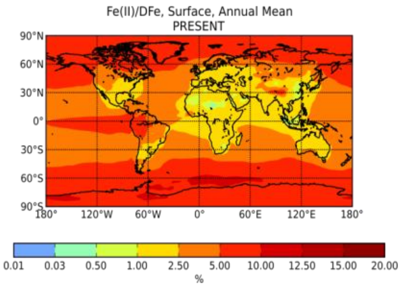

(b)

21) *Figure 8 and Figure S8 are confusing. If Figure 8(e) and 8(f) represent mineral dust only, why the changes in DFe are so large in the Southern Hemisphere? If Figure 8(e) and 8(f) represent the total DFe, what is the difference from Figure S8(a) and S8(b)? Please explain more clearly.*

- We thank the reviewer for finding this double posting and for pointing us the missing caption for figures 8e and 8f. These figures have removed from the main text and are now only in the supplement as Figures S9e and S9f. They show the differences in deposition fluxes of DFe from all sources (combustion, dust and mineral dissolution) – not only mineral dust **-** of PAST and FUTURE from PRESENT simulations.

22) *p.3968, l. 6 and Figure 9: If "to a lesser extent" is true for the Southern Ocean, the large increase is due to the mineral Fe dissolution. This is not true in Figure 8 (a).*

- Following the earlier comments of both reviewers that helped us improve the clarity of the manuscript, this part of the discussion has been rephrased as follows. *"The percentage differences of calculated PRESENT DFe deposition fluxes over oceans from the PAST and FUTURE simulations are depicted in Fig. 9c and 9d, respectively. The model in general calculates for both PAST and FUTURE simulations lower DFe deposition fluxes over oceans. DFe deposition fluxes are calculated to be ~80% higher in the PRESENT than in the PAST simulation (Fig. 9c), which can be attributed both to the increase of i) mineral Fe dissolution (almost 3-fold) and ii) primary DFe emission (from both fossil fuel combustion (6-fold) and biomass burning sources (almost an order of magnitude)). Furthermore, based on emission projections following air quality legislation, decreases of about 30-60% in DFe deposition are calculated for the FUTURE simulation over the Northern Pacific and Atlantic oceans, the Arabian Sea, the Bay of Bengal and the East Mediterranean Sea and lower reductions (less than 20%) over the remote tropical Pacific and Atlantic Oceans and the Southern Ocean These smaller changes from the PRESENT simulation calculated for the FUTURE (globally about 45% reduction) than for the PAST (globally almost 3-fold change) are attributed to the projected increase of Fe biomass burning emissions (about 20%) that partially counterbalance the more than 5-fold reduction in anthropogenic emissions of Fe. Overall, these sensitivity PRESENT-to-FUTURE simulations clearly support that changes in i) atmospheric acidity and ii) Fe combustion sources, both driven by anthropogenic pollutants emissions, affect significantly DFe deposition over the oceans, and therefore they have the potential to also perturb open-ocean phytoplankton growth and thus the carbon biogeochemical cycling."* (lines 1246-1266 in the revised manuscript).

Point-by-point reply to the comments by the reviewer #2

Specific comments:

1) *Page 3969 lines 2-5: "Sensitivity simulations show that increases in anthropogenic emissions since 1850 resulted in more acidic environment and thus an increase (50 %) in DFe deposition (0.230 Tg-Fe yr^{-1} in the past against 0.489 Tg-Fe yr^{-1} nowadays)".*

I can think of at least three changes that can explain the difference in DFe deposition : 1) The biomass burning is increased by a factor of 10 in the model between preindustrial and present-day, 2) Iron is produced from combustion that appeared during the industrial revolution, 3) Atmospheric processing has changed since the atmospheric composition changed radically from preindustrial to present. Hence the reasons for this increase DFe are multiple and the results of the paper give us the combined result from these processes. The authors need to rewrite the conclusions to make sure there is no misinterpretation from the reader. It would have been even a stronger paper if the different causes for the preindustrial to present and the present to future causes for changes had been disentangled.

- Indeed, the changes in the primary emissions of DFe from biomass burning and anthropogenic combustion are also important for the calculated changes in the deposition of DFe. We have rephrased this part in the conclusions to explicitly discuss the role of primary DFe emission changes to the calculated DFe deposition changes. *"Sensitivity simulations show that increases in anthropogenic and biomass burning emissions since 1850 resulted in both enhanced Fe combustion emissions and a more acidic environment and thus more than double DFe deposition (~0.213 Tg-Fe yr^{-1} in the year 1850 against ~0.496 Tg-Fe yr^{-1} nowadays). Air-quality regulations are projected to decrease anthropogenic emissions and thus atmospheric acidity in 2100. Our model results show a 5-fold decrease in Fe emissions from anthropogenic combustion sources (~0.013 Tg-Fe yr^{-1} in the year 2100 against ~0.070 Tg-Fe yr^{-1} nowadays), and about 45% reduction in mineral Fe dissolution (~0.078 Tg-Fe yr^{-1}) compared to the present day (~0.175 Tg-Fe yr^{-1}), while DFe biomass burning emissions are enhanced by 20% (~0.155 Tg-Fe yr^{-1} in the year 2100 against ~0.127 Tg-Fe yr^{-1} nowadays) Overall, the model calculates for 2100 a global DFe deposition of ~0.369 Tg-Fe yr^{-1} that is lower than the present day deposition."* (lines 1329-1340 in the revised manuscript).

- We have also appropriately changed the discussion in section 4.3 and added the following text in the abstract: "*The calculated changes also show that the atmospheric deposition of DFe supply to the globe has more than doubled since the preindustrial period due to 8-fold increases in the primary non-dust emissions and about 3-fold increase in the dust-Fe dissolution flux. However, the DFe* *deposition flux is expected to decrease (by about 25%) due to reductions in the primary non-dust emissions (about 15%) and in the dust-Fe dissolution flux (about 56%). Over the global ocean in present atmospheric deposition of DFe is calculated to be about 3 times higher than for 1850 emissions and about 30% decrease is projected for 2100 emissions. These changes are expected to impact most on the High Nutrient Low Chlorophyll oceanic regions."* (lines 48-54 in the revised manuscript).

2) *For the aspect of presentation, the Figures that 2D-maps (Fig. 2, 3, 4, 6, 8 & 9) are much too small to be captured by the naked eye. The reader has to use magnifying glasses to see them. An effort should be put on these Figures, together with the presentation of Fig. 5 that permits to evaluate the model against observations.*

- We have tried to improve the readability of the Figures. In particular we have increased the fonts in Figure 5, since they were indeed very small. The other figures are of good quality and they can be magnified as needed to fit the full page available when they will be inserted in the main text for the final edited manuscript. In addition the journal is electronic which allows the magnification of any figure before printing.

3) *The authors' state that the comparison with the Atlantic Ocean TFe deposition is satisfying (Figures 7a through d). They should comment on the very large overestimate seen in Regions 2 and 3 in the periods April-May-June and Sept-Oct.-Nov. Such difference with the observations of Baker et al. (2013) needs to be resolved or at least noticed to try to advance our understanding of dissolved iron*.

- Both regions 2 and 3 are strongly affected by Sahara dust outflow. Thus the model overestimate of TFe observations by Baker et al. (2013), while DFe observations are much better captured by the model, could be due to a longer lifetime of TFe in the model than in the atmosphere resulting from smaller size distributions of TFe in the model than in reality. Note also that these estimates are associated with large uncertainty. This is now discussed in section 3.6 (lines 998-1002 in the revised manuscript).

4) *The regions in Figure 4c where the ratio of %Fe(II)/DFe is greater than 10% are regions for which dust concentrations are very small and this should be explicitly noted in the text.*

- We rephrased as: *"This ratio also exceeds ~10% at several other locations around the globe, in particular over the tropical Pacific and the Southern Ocean; implying that chemical aging of dust due to atmospheric processing and long-range transport enhances significantly the production of Fe(II). As also discussed* *in Sec. 2.6, in relatively basic pH environments (e.g the Southern Ocean due to the buffering capacity of sea-salt particles; see Fig. S2) and due to high OXL concentrations (e.g. tropical Pacific ocean) the production of Fe(II) is favoured (Fig. S4e and Fig. S4h, respectively). Thus, our model calculations indicate that the enhanced fraction of Fe(II) over the remote oceans (Fig. 4c), characterized by low concentrations of dust and non-negligible OXL concentrations (see Fig. S3) due to the aqueous-phase oxidation of organic compounds of marine origin NMVOCs (e.g. isoprene) could be attributed to the production of ferrous-oxalato complexes."* (lines 790-833 in the revised manuscript).

Minor comments:

1) *Page 3496, line 15: change, ''At the surface waters, the phytoplankton photosynthetic activity uses* CO_2 *and nutrients. . ." to "In surface waters, the phytoplankton photosynthetic activity uses* CO_2 *and nutrients. .."*

- Corrected (line 94 in the revised manuscript).

2) *Page 3947 line 20 : ''3% of Hematite in dust" please indicate if this content refers to mass or to volume.*

- Clarification has been added and typo corrected (see also Reply to rev. #1). It now reads: '5% mass fraction of Hematite in dust' (lines 157-158 in the revised manuscript).

3) *Page 3948, lines 3 to 6 : '' However, the large acid buffering ability of the carbonate from minerals like CaCO3 and MgCO3 in coarse dust particles can regulate mineral-Fe proton promoted dissolution, creating an inverse relationship between SFe and particle size (Ito and Feng, 2010). " There is much debate about the cause for this inverse relationship, several factors are at play and mineral-Fe proton promoted dissolution is just one of them. Be more conservative when putting this cause forward.*

- This sentence has been rephrased as follows: '*However, the buffering capacity of minerals like* $CaCO_3$ *and* $MgCO_3$ *which reside in coarse dust particles may regulate mineral-Fe proton-promoted dissolution, contributing, among others together with combustion emissions of DFe on fine particles and atmospheric transport, to the observed an inverse relationship between SFe and particle size (Ito and Feng, 2010)*' (lines 171-190 in the revised manuscript).

4) *You use a model resolution of 6◦ in longitude by 4◦ in latitude (line 27 page 3950). You should state that this coarse resolution will smooth the gradient in dust and Fe concentrations in or near-source regions.*

- We agree with the reviewer that the highest is the spatial resolution of the model, the more accurate are the results. Therefore, for the revised version of this paper, we have performed the simulations in the fine resolution of the model (3x2 with 34 hybrid levels in the vertical). About 50% of uncertainty in the computed atmospheric deposition is associated with the model horizontal resolution. A comment has been added in section 3.5: *"In addition, at least a 50% of uncertainty in the calculated deposition fluxes was found to be associated with the applied horizontal resolution of the model, with higher fluxes calculated with the higher model resolution."* (lines 933-936 in the revised manuscript).

5) *Page 3952, line 6 The iron-content for hematite and goethite differ by 7% (62.8% for goethite and 69.94% for hematite (see http://webmineral.com), this is worth taking into account rather than using the same content of 66% in your computations.*

- The Nickovic et al. (2012) mineralogy database that we are using provides the distribution of the sum of Hematite and Goethite (as iron oxides) with a mean iron-content of 66%. Therefore we do not have the information needed to split the database in hematite and goethite. However, a relevant comment has been added in section 2.2: *"Despite differences in the chemical reactivity and iron content of goethite and hematite (e.g. see http://webmineral.com), these minerals are here considered as one surrogate species, the hematite, used as proxy for Fe oxides as suggested by Nickovic et al. (2012)*." (lines 356-359 in the revised manuscript).

6) *In Table 1, you have to clearly point out that it is a Fe content that you refer to and not the relative abundance of the mineral in dust. I got confused by it the first time I read through this Table.*

- To avoid confusion, the title of this Table has been modified and it is now clearly stated that the emissions of Iron contained in dust minerals are shown.

7) *Page 3957 lines 14-15: Please indicate the percentage of content of Fe in dust that is calculated here (as a global mean).*

- In section 2.2, first paragraph, we mention that:
  "*Given this, the annual global mean Fe content of emitted dust particles in TM4-ECPL is calculated to be ∼3.2 %* " (lines 355-356 in the revised manuscript).

8) *In paragraph 3.5 the maximum values of deposition you give are strongly linked to the model resolution. With a higher model resolution, your values would be increased. It is worth mentioning it here.*

- see reply to comment 4.

9) *Page 3967, bottom of page: What method did you use to delimit the HNLC regions?*

- For the characterisation of the HNLC oceanic regions for the present study, the annual mean global NO_3^- surface water concentrations from the LEVITUS94 World Ocean Atlas (http://iridl.ldeo.columbia.edu/SOURCES/ .LEVITUS94/) and the monthly chlorophyll a (Chl a) concentrations MODIS retrievals taken into account in the model (Myriokefalitakis et al., 2010) for the year 2008 have been used. As we explain in p. 3967 line 16 of the discussion paper (1st paragraph section 4.3) the model grid boxes corresponding to HNLC waters are here defined based on the co-occurrence of surface seawater NO_3^- concentrations of > 4 μM (Duce et al., 2008) and Chl-a concentrations of < 0.1 mg m^{-3} (Boyd et al., 2007). This is an off-line calculation and the figure of HNLC regions as delimited for the present study is now added in the supplement – New figure S7e.

Changes in dissolved iron deposition to the oceans driven by human activity: a 3-D global modelling study

S. Myriokefalitakis[1], N. Daskalakis[1,2], N. Mihalopoulos[1,3], A. R. Baker[4], A. Nenes[2,5,6], and M. Kanakidou[1]

[1]{Environmental Chemical Processes Laboratory, Department of Chemistry, University of Crete, P.O. Box 2208, 70013 Heraklion, Greece}

[2]{Institute of Chemical Engineering Sciences (ICE-HT), FORTH, Patras, Greece}

[3]{Institute for Environmental Research and Sustainable Development, National Observatory of Athens, Athens, Greece}

[4]{School of Environmental Sciences, University of East Anglia, Norwich UK, NR4 7TJ}

[5]{School of Earth and Atmospheric Sciences, Georgia Institute of Technology, 311 Ferst Drive, Atlanta, GA 30332-0100, USA}

[6]{School of Chemical and Biomolecular Engineering, Georgia Institute of Technology, 311 Ferst Drive, Atlanta, GA 30332-0100, USA}

Correspondence to: S. Myriokefalitakis (stelios@uoc.gr); M. Kanakidou (mariak@uoc.gr)

Deleted: stelios@chemistry.uoc.gr

Deleted: mariak@chemistry.uoc.gr

Abstract

The global atmospheric iron (Fe) cycle is parameterized in the global 3-D chemical transport model TM4-ECPL to simulate the proton- and the organic ligand-promoted mineral Fe dissolution as well as the aqueous-phase photochemical reactions between the

oxidative states of Fe (III/II). Primary emissions of total (TFe) and dissolved (DFe) Fe associated with dust and combustion processes are also taken into account, with TFe mineral emissions calculated to amount to ~35 Tg-Fe yr^{-1} and TFe emissions from combustion sources to ~2 Tg-Fe yr^{-1}. The model reasonably simulates the available Fe observations, supporting the reliability of the results of this study. Proton- and organic ligand-promoted Fe-dissolution in present-day TM4-ECPL simulations is calculated to be ~0.175 Tg-Fe yr^{-1}, approximately half of the calculated total primary DFe emissions from mineral and combustion sources in the model (~0.322 Tg-Fe yr^{-1}). The atmospheric burden of DFe is calculated to be ~0.024 Tg-Fe. DFe deposition presents strong spatial and temporal variability with an annual flux of ~0.496 Tg-Fe yr^{-1}, from which about 40% (~0.191 Tg-Fe yr^{-1}) are deposited over the ocean. The impact of air-quality on Fe deposition is studied by performing sensitivity simulations using preindustrial (year 1850), present (year 2008) and future (year 2100) emission scenarios. These simulations indicate that an about 3 times increase in Fe-dissolution may have occurred in the past 150 years due to increasing anthropogenic emissions and thus atmospheric acidity. Air-quality regulations of anthropogenic emissions are projected to decrease atmospheric acidity in the near future reducing to about half the dust-Fe dissolution relative to the present-day. The organic ligand contribution to Fe dissolution shows an inverse relationship to the atmospheric acidity, thus its importance has decreased since the preindustrial period but is projected to increase in the future. The calculated changes also show that the atmospheric DFe supply to the globe has more than doubled since the preindustrial period due to 8-fold increases in the primary non-dust emissions and about 3-fold increase in the dust-Fe dissolution flux. However, in the future the DFe deposition flux is expected to decrease (by about 25%) due to reductions in the primary non-dust emissions (about 15%) and in the dust-Fe dissolution flux (about 55%). Over the global ocean in present atmospheric deposition of DFe is calculated to be about 3 times higher than for 1850 emissions and about 30% decrease is projected for 2100 emissions. These changes are expected to impact most on the High Nutrient Low Chlorophyll oceanic regions.

Deleted: .

Deleted: are

Deleted: Accounting for proton

Deleted: , the total Fe-dissolution

Deleted: 163

Deleted: that accounts for up to ~50%

Deleted: .

Deleted: 012

Deleted: deposition

Deleted: about

Deleted: 489

Deleted: 25

Deleted: 124

Deleted: ,

Deleted: (~2 times)

Deleted: On the opposite, a decrease (~2 times) of Fe-dissolution is projected for near future, since atmospheric acidity is expected to be lower than present-day due to air

Deleted: .

Deleted: High-Nutrient-Low-Chlorophyll oceanic areas (HNLC) characterized by Fe scarcity,

Deleted: increased (~50%)

Deleted: . However,

Deleted: (~30%) to almost preindustrial levels over the Northern Hemisphere HNLC oceanic regions in the future. Significant

Deleted: of ~20% over the Southern Ocean and the remote tropical Pacific Ocean are also projected which can further limit

Deleted: productivity over HNLC waters

1 Introduction

Atmospheric deposition of trace constituents, both of natural and anthropogenic origin, can act as a nutrient source into the open ocean and therefore can affect marine ecosystem functioning and subsequently the exchanges of CO_2 between the atmosphere and the global ocean (Duce et al., 2008). In surface waters, the phytoplankton photosynthetic activity uses CO_2 and nutrients to produce biomass and is responsible for nearly half of annual CO_2 exchange with the deep-ocean that contains ~85% of Earth's mobile carbon (Shao et al., 2011). This is the so-called 'biological pump', where the deeper the carbon sinks, the longer it will be removed from the atmosphere (Falkowski et al., 2000). The net result of the biological pump is a continual atmospheric carbon transfer to the deep ocean. Aeolian dust deposition, calculated to be ~1257 Tg yr^{-1} (median of 15 global models by Huneeus et al., 2011), contains ~3.5% iron (Fe) on average, and it is the most significant external supply of Fe (as a micronutrient) in surface waters (Taylor and McLennan, 1985; Mahowald et al., 2005; 2009). Fe scarcity limits phytoplankton productivity in High-Nutrient-Low-Chlorophyll (HNLC) regions (i.e. the Southern Ocean, the Eastern equatorial and the Subarctic Pacific; Boyd et al., 2005) and thus primary productivity in large portions of the global ocean, affecting significantly the biological carbon export at global scale (Maher et al., 2010). The correlation of Fe supply and atmospheric CO_2 trapping to the ocean, forms the so-called "Iron Hypothesis" (Martin and Fitzwater, 1988) that initiated significant scientific debate on the potential use of Fe to fertilize the global ocean (i.e. geo-engineering) and consequently increase CO_2 storage in the ocean (e.g. Moore and Doney, 2007).

The bioavailable form of Fe that is acquired by phytoplankton is associated with the soluble fraction of Fe, which experimentally is measured as the fraction filterable through 0.2-0.45 μm filters (Kraemer, 2004). Aerosols are emitted or formed, transported and deliquesce in the atmosphere (Raes et al., 2000). Processes that occur in the water associated with aerosols can change aerosol properties. There is experimental evidence that atmospheric acidity is increasing dust solubility (e.g. Nenes et al., 2011) and that present-day atmospheric acidity is mainly driven by air pollution (Seinfeld and Pandis,

Deleted: ¶

Deleted: Aeolian dust deposition is calculated to be ~1257 Tg yr^{-1} (median of 15 global models by Huneeus et al., 2011) and containing ~3.5% Fe on average is the most significant external supply of iron (Fe

Moved down [1]:) in surface waters (Taylor and McLennan, 1985; Mahowald et al., 2005; 2009).

Deleted: As a micronutrient, Fe is limiting phytoplankton productivity in the High-Nutrient-Low-Chlorophyll (HNLC) oceanic regions (i.e.

Moved down [2]: the Southern Ocean, the Eastern equatorial and the Subarctic Pacific; Boyd et al.,

Deleted: 2005). The supply of Fe-bearing dust can thus limit primary productivity in large portions of the global ocean, affecting significantly the biological carbon export at the

Moved down [3]: global scale (Maher et al., 2010).

Deleted: At the

Moved (insertion) [1]

Moved (insertion) [2]

Moved (insertion) [3]

Deleted: to

Deleted: , deliquesce

1998 and references therein). Although the fraction of soluble Fe in soil is low (~0.1%; Mahowald et al., 2009 and references therein); atmospheric chemical processes are responsible for Fe conversion to more soluble forms (Mahowald et al., 2009), and thus bioavailable form for the ocean biota. Dust coating by acidic–soluble materials (e.g. nitrates, sulphates) alters also the global pattern of Fe deposition (Fan et al., 2004).

Significant scientific effort has been made to understand the impact of anthropogenically driven atmospheric acidity on dust and parameterise it in global models. To study the aforementioned changes in dust-Fe solubility driven by human activities, atmospheric models need to account for both i) the composition of the Fe source and ii) the atmospheric aging of dust. However, the atmospheric chemical aging of dust with respect to dissolved/bioavailable Fe (hereafter DFe) production is parameterized in chemistry-transport models (CTMs) in different ways. In the modelling study of Meskhidze et al. (2005) hematite (Fe_2O_3) was considered as the only Fe-containing mineral in dust (5% mass fraction of hematite in dust) and the proton-promoted Fe dissolution was described using the empirical parameterisation developed by Lasaga et al. (1994). That study simulated the production of DFe in the ferric oxidation state (Fe(III)) but did not account for any photochemical cycling between Fe(III) and Fe(II). Luo et al. (2008) using the same approximation considered the formation of DFe in the ferrous form (Fe(II)) during Fe-containing minerals dissolution. In support of the proton-promoted Fe dissolution hypothesis, a positive correlation of Fe solubility (hereafter SFe; SFe = 100×DFe/TFe) and sulphur emissions has been observed for acidic atmospheric samples collected at urban sites (Oakes et al., 2012). The simulations by Solmon et al. (2009) suggest that doubling of sulphur emissions can increase the proton-promoted dissolution and deposition of dissolved Fe to the remote Pacific Ocean by ~13%.

Fe dissolution from minerals under acidic conditions occurs on different timescales; from hours to weeks depending on the size and the type of the Fe-containing mineral (Shi et al., 2011a). However, the buffering capacity of minerals like $CaCO_3$ and $MgCO_3$ which reside in coarse dust particles may regulate mineral-Fe proton-promoted dissolution, contributing, among others together with combustion emissions of DFe on fine particles

Deleted: ;

Deleted: 2005

Deleted: the

Deleted: dissolve

Deleted: Hematite

Deleted: 3%

Deleted: Hematite

Deleted: =

Deleted: in

Deleted: 2011

Deleted: large acid

Deleted: ability

Deleted: the carbonate from

Deleted: can

Deleted: creating

and atmospheric transport, to the observed an inverse relationship between SFe and particle size (Ito and Feng, 2010). A recent CTM study (Ito and Xu, 2014) simulated the present-day SFe over the Northern Hemisphere oceans reasonably well, and calculated the proton-promoted dissolution of Fe in the year 2100, considering three pools of Fe-containing minerals depending on their timescale of potential for Fe dissolution based on the findings of Shi et al. (2011b; 2012).

Laboratory studies have also shown the occurrence of photoinduced reductive Fe dissolution under rather acidic conditions (e.g. pH < 4), suggesting a steady state Fe(II) production during exposure of dust to solar radiation and thus, increased daytime dissolution rate of hematite compared to standard kinetics (Zhu et al., 1993; Jickells and Spokes, 2001 and references therein). However, the dust-Fe dissolution through photoreduction has only limited impact (<1%) on the DFe concentration (Zhu et al., 1993). Moreover, experimental data also support that both inorganic (e.g. sulphuric and nitric acid) and organic (e.g. oxalic and acetic acid) acids can increase Fe dissolution (Paris et al., 2011; Paris and Desboeufs, 2013). Laboratory investigations (Chen and Grassian, 2013) also indicate that the relative capacity of oxalic acid in acidic solution (pH = 2) is by far the most important for Fe dissolution in dust and combustion aerosols compared to sulphuric acid due to the formation of mononuclear bidentate ligand with surface Fe, in contrast to the weaker complexes formed from HSO_4^- and SO_4^{2-}.

Oxalic acid/oxalate (hereafter OXL) is globally the most abundant dicarboxylic acid, formed via chemical oxidation of both biogenic and anthropogenic gas-phase precursors in the aqueous phase of aerosols and cloud droplets (e.g. Carton et al., 2007; Lim et al., 2010). Johnson and Meskindze (2013) calculated that the ligand (OXL)-promoted Fe dissolution and Fe(II)/Fe(III) redox cycling of Fe-content of mineral dust in both aerosol and cloud water, increased total annual calculated DFe deposition to global oceanic regions by ~75%, compared to only proton-promoted Fe dissolution simulations. However, the aforementioned study used sulphate aerosol as a proxy for the occurrence of OXL and took into account three Fe-containing dust-minerals (i.e. goethite, hematite and illite) as studied by Paris et al. (2011). A recent modelling study by Ito (2015),

Deleted: predicted

Deleted: 2011

Deleted: Hematite

Deleted: sulphate, ammonium

Deleted: nitrate

Deleted: oxalate) ligands

Deleted: as

Formatted: Space Before: 12 pt, Line spacing: 1.5 lines

Deleted:

Deleted: -

Deleted: that

published after the submission of the present work, focusing on the atmospheric processing of Fe-containing combustion aerosols by photochemical reactions with inorganic and organic acids indicates that ligand (OXL)-promoted Fe dissolution more than doubles the calculated DFe deposition from combustion sources over certain regions of the global ocean.

Besides proton- and ligand- promoted mineral-Fe dissolution, primary emissions of Fe, especially from combustion processes can lead to an increase in the SFe fraction. Mineral-Fe represents ~95% of the global atmospheric TFe source, with combustion Fe sources responsible for the remaining ~5% (Luo et al., 2008; Mahowald et al., 2009). Luo et al. (2008) accounted for both soluble and insoluble forms of Fe emissions from biomass burning and anthropogenic combustion processes in relation to Black Carbon (BC) emissions and they estimated (based on observed Fe/BC ratios) that ~1.7 $Tg\text{-}Fe\cdot yr^{-1}$ are emitted to the atmosphere via combustion processes. Mahowald et al. (2009) also indicate that humans may significantly impact DFe deposition over oceans by increasing both the acidity of atmospheric aerosol, as well as the DFe emissions from combustion processes. Model projections for the year 2100 suggest that fossil fuel combustion aerosols from shipping could contribute up to ~60% of DFe deposition to remote oceans (Ito, 2013).

Deleted: In addition to

Deleted: Mahowald et al. (2008) estimated that although mineral

Deleted: of iron are

Deleted: %. In addition, the same study suggested that humans may significantly impact DFe deposition over oceans by increasing both the acidity of atmospheric aerosol, as well as the DFe emissions from combustion.

Deleted: .

Deleted: further

Deleted: in

Deleted: ,

Deleted: which ~4% as DFe from all

Deleted: also indicate

In the present study, the 3-D chemical transport global model TM4-ECPL that explicitly calculates aqueous-phase chemistry of OXL and the photochemical cycle of the atmospheric Fe cycle is used to simulate the Fe deposition over land and oceans, accounting for five Fe-containing dust minerals and for anthropogenic emissions of Fe. Following the scheme of Ito and Xu (2014), dissolution of Fe (Section 2) from 3 pools of minerals (Shi et al., 2012) is here considered to occur by proton-promoted dissolution at three characteristic time scales and by ligand (OXL)-promoted dissolution (as demonstrated by Paris et al., 2011 and parameterized by Johnson and Meskindze, 2013). The calculated TFe and DFe global atmospheric budgets and distributions are presented and compared to observations in Section 3. The importance of air-pollutants for DFe atmospheric concentrations and deposition is investigated in Section 4, based on

Deleted:

Deleted: on

simulations using past and future anthropogenic and biomass burning emissions scenarios. The significant contribution of anthropogenic sources to the dissolution of Fe-containing minerals, their impact on DFe deposition over oceans and the implications of the findings for the biogeochemistry of marine ecosystems are summarized in section 5.

Deleted: solubilization

Deleted: Fe

Deleted: finding

2 Model description

The TM4-ECPL global chemistry – transport model (Myriokefalitakis et al., 2011; Daskalakis et al., 2015 and references therein) is able to simulate oxidant ($O_3/NO_x/HO_x/CH_4/CO$) chemistry, accounting for non – methane volatile organic compounds (NMVOCs, including isoprene, terpenes and aromatics), as well as all major aerosol components, including secondary aerosols like sulphate (SO_4^{2-}), nitrate (NO_3^-), ammonium (NH_4^+) using ISORROPIA II thermodynamic model (Fountoukis and Nenes, 2007) and secondary organic aerosols (SOA) (Tsigaridis and Kanakidou, 2003, 2007). Compared to its parent TM4 model (van Noije et al., 2004), the current version has a comprehensive description of chemistry (Myriokefalitakis et al., 2008) and organic aerosols (Myriokefalitakis et al., 2010). It also accounts for multiphase chemistry in clouds and aerosol water that produces OXL and affects SOA formation (Myriokefalitakis et al., 2011).

Deleted: 2014

Deleted: sulfate

For the present study, TM4-ECPL is driven by ECMWF (European Center for Medium – Range Weather Forecasts) Interim re–analysis project (ERA – Interim) meteorology (Dee et al., 2011). Advection of the tracers in the model is parameterized using the slopes scheme (Russell and Lerner, 1981 and references therein). Convective transport is parameterized based on Tiedke (1989) and the Olivie et al. (2004) scheme. Vertical diffusion is parameterized as described in Louis (1979). For wet deposition, both large scale and convective precipitation are considered. In-cloud and below cloud scavenging is parameterized in TM4-ECPL as described in detail by Jeuken et al. (2001). In-cloud scavenging of water soluble gases is calculated accounting for the solubility of the gases (effective Henry law coefficients; Tsigaridis et al., 2006; Myriokefalitakis et al., 2011 and

Deleted: The vertical

Deleted:).

references therein). Dry deposition for all fine aerosol components is parameterized similarly to that of nss-SO_4^{2-}, which follows Tsigaridis et al. (2006). Gravitational settling (Seinfeld and Pandis, 1998) is applied to all aerosol components and is an important dry deposition process for coarse particles like dust and sea-salt. The current model configuration has a horizontal resolution of 3° in longitude by 2° in latitude and 34 hybrid layers in the vertical, from surface up to 0.1 hPa. All simulations have been performed with meteorology of the year 2008 and a model time-step of 30 min.

Deleted: the main

Deleted: 6°

Deleted: 4°

2.1 Emissions

TM4-ECPL uses the anthropogenic and biomass burning emissions (NMVOC, nitrogen oxides (NOx), CO, SO_2, NH_3, particulate organic carbon (OC) and black carbon (BC)) from the ACCMIP database (Lamarque et al., 2013; http://eccad.sedoo.fr/eccad_extract_interface/JSF/page_meta.jsf). Biogenic emissions (isoprene, terpenes, acetaldehyde, acetone, ethane, ethene, propane, propene, formaldehyde, CO, methyl – ethyl ketone, toluene, methanol) come from the MEGAN – MACC Biogenic Emission Inventory for the year 2008 (Sindelarova et al., 2014). Soil NOx and oceanic emissions (CO, ethane, ethene, propane, propene) are taken from the POET (Granier et al., 2005) inventory database (http://eccad.sedoo.fr). Oceanic emissions of primary organic aerosol, isoprene, terpenes and sea – salt particles are calculated online driven by meteorology following Myriokefalitakis et al. (2010). Dust emissions are obtained from the daily AEROCOM inventories (Aerosol Comparison between Observations and Models; Dentener et al., 2006) updated to the year 2008 (E. Vignati, pers. com., 2011). The anthropogenic and biomass burning emissions (NMVOC, NOx, CO, SO_2, NH_3, OC and BC) from the ACCMIP database (Lamarque et al., 2013) for the years: 1850 (hereafter PAST), 2008 (hereafter PRESENT) and for the year 2100 based on the RCP6 emission scenario (hereafter FUTURE), have been used for the different simulations as further explained. A summary of the emissions considered in the model is given in Table S1 in the supplementary material.

Deleted: (2010) and Vignatti et al.

Deleted: table

Deleted: of dust and Fe-containing minerals used in the TM4-ECPL model is provided in Table 1 (all other emissions

Deleted: are

Deleted:).

2.2 Dust iron-containing minerals emissions

Various Fe-containing clay minerals (illite, kaolinite and smectite), oxides (hematite and goethite) and feldspars can be found in mineral dust (Nickovic et al., 2013). In the present study, the global soil mineralogy dataset developed by Nickovic et al. (2012) at 30” resolution (~1 km) has been initially re-gridded to 1°x1° global resolution and applied to the 1°x1° daily dust emissions taken into account by TM4-ECPL. The percentage content in Fe of the different Fe-containing minerals of dust that are considered in the model has been taken from Nickovic et al. (2013) (illite 4.8%, kaolinite 0.7%, smectite 16.4%, goethite and hematite 66% and feldspar 2.5%). Given this, the annual global mean Fe content of emitted dust particles in TM4-ECPL is calculated to be ~3.2%. Despite differences in the chemical reactivity and iron content of goethite and hematite (e.g. see http://webmineral.com), these minerals are here considered as one surrogate species, the hematite, used as proxy for Fe oxides as suggested by Nickovic et al. (2012).

Based on the aforementioned soil mineralogy database (F_{MIN_DUST}), the daily dust emissions ($Dust_{Emi}$) in the model and the Fe content of the minerals (F_{Fe_MIN}), TM4-ECPL calculates the TFe emissions (Fe_{Emi}) from soils as:

$$Fe_{Emi} = Dust_{Emi} \cdot F_{Min\_Dust} \cdot F_{Fe\_Min} \qquad (1)$$

Thus, the model accounts for the following annual Fe emissions from soils: ~8.473 Tg-Fe yr^{-1} from illite, ~0.871 Tg-Fe yr^{-1} from kaolinite, ~17.154 Tg-Fe yr^{-1} from smectite, ~5.663 Tg-Fe yr^{-1} from hematite and goethite and ~2.761 Tg-Fe yr^{-1} from Feldspars (Table 1), total ~35.048 Tg-Fe yr^{-1}. The DFe emissions in the form of impurities in soils are prescribed in the initial dust sources as 4.3% on kaolinite and 3% on feldspars as suggested by Ito and Xu (2014) and account for ~0.125 Tg-Fe yr^{-1}. A summary of dust and Fe-containing minerals emissions used in the TM4-ECPL model is provided in Table 1. The annual mean spatial distributions of dust (Fig. S1a) and emissions of Fe contained in different minerals (Fig. S1b-f) as calculated by the model are also shown in the supplement.

2.3 Anthropogenic and biomass burning iron emissions

Deleted: 7.9

Deleted: Illite

Deleted: 9

Deleted: Kaolinite, ~16.1

Deleted: Smectite

Deleted: 7

Deleted: Hematite and Goethite and ~2.8 Tg-Fe yr^{-1} Feldspar

Deleted: 34

Deleted: Kaolinite

Deleted: Feldspar

Deleted: 12 Tg-Fe yr^{-}

Deleted: average surface

Deleted: concentrations

Deleted: concentrations

Deleted: Figure S1 in

TFe emissions from combustion sources have been estimated at 1.07 Tg-Fe yr^{-1} from biomass burning, 0.66 Tg-Fe yr^{-1} from coal combustion (Luo et al., 2008) and ~0.016 Tg-Fe yr^{-1} from shipping (Ito et al., 2013), all for the year 2001. For this work, global and monthly mean scaling factors of TFe emissions to those of BC (Fe/BC) for each of the above mentioned emission sectors have been derived based on emission estimates provided by Luo et al. (2008) and the BC sources from the ACCMIP database for the year 2001. Furthermore, to calculate the DFe in primary emissions (both in fine and coarse particles), the DFe emission estimates by Ito (2013) of 0.127 Tg-Fe yr^{-1} from biomass burning, 0.055 Tg-Fe yr^{-1} from coal combustion and 0.013 Tg-Fe yr^{-1} from shipping, have been used together with the TFe emissions above mentioned for the year 2001 (Luo et al., 2008) to derive mean solubility for each of these three emission categories. These are ~12% for biomass burning Fe sources, ~8% for coal combustion and ~81% for shipping. The derived Fe/BC emission ratios and the mean Fe solubility per source category are then applied to the BC emissions from the ACCMIP database for the respective year, to compute the PAST, PRESENT and FUTURE emissions of TFe and DFe. The computed annual mean surface distributions of the TFe emitted by anthropogenic emissions (including shipping), and biomass burning used in the model (~1.983 Tg-Fe yr^{-1} for the year 2008) are depicted in Fig. S1g and S1h, respectively.

2.4 Mineral dissolution scheme

The model calculates the dissolution of Fe-containing minerals in the aerosol water and in the cloud droplets. TM4-ECPL treats the Fe dissolution as a kinetic process that depends on the concentrations of i) H^{+} (proton-promoted Fe dissolution**)** and ii) OXL (organic ligand-promoted Fe dissolution) in the solution (Fig. 1).

2.4.1 Proton-promoted iron dissolution

The proton-promoted dissolution rate of minerals in aerosol and cloud water is calculated by applying the empirical parameterization developed by Lasaga et al. (1994), taking into account the saturation degree of the solution, the type of each mineral (MIN), as well as the reactivity of Fe species and the ambient temperature.

Deleted: Anthropogenic

Deleted: of TFe

Deleted: and

Deleted: Tg-Fe

Deleted:),

Deleted: -emissions

Deleted: 5

Deleted: both

$$R_{Fe} = NFe_{MIN} \cdot K_{MIN}(T) \cdot a(H^{+})^{m} \cdot f_{MIN} \cdot A_{MIN} \qquad (2)$$

where R_{Fe} is the Fe-containing mineral dissolution rate (moles of Fe per gram of MIN per s), NFe_{MIN} is the number of moles of Fe per mole of mineral, K_{MIN} is the temperature (T) dependent dissolution reaction coefficient of the mineral (mol m^{-2} s^{-1}), $\alpha(H^{+})$ is the H^{+} activity in the solution, m is the reaction order with respect to aqueous-phase protons, A_{MIN} is the specific surface area of the mineral (m^{2} g^{-1}) and f_{MIN} accounts for the variation of the rate when deviating from equilibrium. For the present study the above formulation is applied to each mineral concentration *[MIN]* (and not to the bulk mass of dust aerosol), since the model describes each mineral with a different tracer in the chemical scheme. For the calculation of the deviation from equilibrium f_{MIN}, the Eq. (3) given by Ito and Xu (2014) is used:

$$f_{MIN} = 1 - (a_{Fe^{3+}} \cdot a_{H^{+}}^{-n_{MIN}}) / Keq_{MIN} \qquad (3)$$

where $a_{Fe^{3+}}$ is the concentration of Fe(III) in the aqueous solution (mol L^{-1}), n_{MIN} is the stoichiometric ratio (number of moles mobilized per mole of mineral) and Keq_{MIN} is the equilibrium constant for iron oxides formation ($Fe(OH)_3$). Mineral dissolution rates and the related factors used in this study are listed in Table 2, separating between the DFe (attributed to the emissions), fast released iron (Fe_f), intermediate released iron (Fe_I) and refractory iron (Fe_R) (Shi et al., 2011b; 2012) as explicitly parameterized by Ito and Xu (2014). Aerosol water pH is calculated by the ISORROPIA II thermodynamic model which solves the K^{+}–Ca^{2+}–Mg^{2+}–NH_4^{+}–Na^{+}–SO_4^{2-}–NO_3^{-}–Cl^{-}–H_2O aerosol system. Based on the composition of mineral dust and sea-salt elements, ISORROPIA II in TM4-ECPL takes into account the following mean percent mass content of particles: Na^{+}: 30.6% on sea-salt and 1.7% on dust, Ca^{2+}: 1.2% on sea-salt, K^{+}: 2.4% on dust and 1.1% on sea-salt and Mg^{2+}: 1.5% on dust (as magnesite; Ito and Feng, 2010 - consistent with Formenti et al., 2008 observations) and 3.7% on sea-salt (http://geology.utah.gov/online_html/pi/pi-39/pi39pg9.htm), Cl^{-}: 55% on sea-salt and SO_4^{2-}: 7.7% on sea-salt. The global soil mineralogy dataset (Nickovic et al., 2012) has

Deleted: equation

Moved (insertion) [4]

Deleted: In order to account for potential neutralization of the acidic species by dust carbonate minerals, dust crustal materials are also taken into account for this study.

Deleted: elements

Deleted: 8

Deleted: 4.4% on dust (as calcite; Meskidze et al., 2005) and

Deleted: .5

been applied on dust emissions to calculate the concentrations of Ca^{2+} on dust particles (i.e. calcite ($CaCO_3$) and gypsum ($CaSO_4$)).

Aerosol pH and water are here calculated for each aerosol mode (Fig. S2a for the fine mode and Fig. S2b for the coarse mode). The pH values for each aerosol mode are calculated by the thermodynamic equilibrium model ISORROPIA II assuming internal mixing of the aerosols (Fountoukis and Nenes, 2007). Briefly, for each mode (fine and coarse) sulphate, nitrate, ammonium and sea-salt (i.e. K^+; Ca^{2+}; Mg^{2+}; Na^+; SO_4^{2-}; Cl^-) aerosols are assumed to be internally mixed. Carbonates ($CaCO_3$, $MgCO_3$) and gypsum ($CaSO_4$) are considered to be present in the silt soil particles (Meskhidze et al., 2005), with their impact on the coarse particulate H^+ and H_2O, to be calculated interactively by the ISORROPIA II. The dissolved Ca^{2+} and Mg^{2+} is distributed by the thermodynamic model among all possible solids.

In TM4-ECPL, in-cloud pH (Fig. S2c at ~850hPa and Fig. S2d for zonal mean) is controlled by strong acids (sulphates, SO_4^{2-}; methanesulphonate, MS^-; nitric acid, HNO_3; nitrate ion, NO_3^-), bases (ammonium ion, NH_4^+), as well as by the dissociations of hydrated CO_2, SO_2, NH_3 and of oxalic acid (Myriokefalitakis et al., 2011). Crustal and sea-salt elements are not considered for pH calculations in the cloud chemical scheme.

2.4.2 Organic ligand-promoted iron dissolution

Recent laboratory studies show a positive linear correlation between iron solubility and organic ligands concentrations (e.g. Paris and Desboeufs, 2011 and references therein). Two mechanisms have been proposed concerning the mineral dissolution in the presence of organic ligands: i) the non-reductive (Stumm and Morgan, 1996) and ii) the reductive (Stumm and Sulzberger, 1992) ligand-promoted dissolution. Experimental studies by Paris and Desboeufs (2013) indicate that certain organic ligands (including OXL) enhance Fe dissolution from mineral dust. This ligand-promoted dissolution was accompanied by increased concentrations of dissolved Fe(II) and was probably related to the ability of organic ligands to act as electron donors.

Deleted: the

Deleted:) and

Deleted: and

Deleted: weak electrolytes. For pH > 4.3

Deleted: dissolution and subsequent dissociation

Deleted: OXL are also taken into account

Deleted: Note that crustal

Deleted: species

Moved up [4]: Mineral dissolution rates and the related factors used in this study are listed in Table 2, separating between the DFe (attributed to the emissions), fast released iron (Fe_f), intermediate released iron (Fe_I) and refractory iron (Fe_R) (Shi et al.,

Deleted: 2011; 2012) as explicitly parameterized by Ito and Xu (2014).

Formatted: Font: Bold, Not Italic

Formatted: Font: Bold

Deleted: present

Deleted: ;

Deleted: experimental studies support

Deleted: the released

Deleted: by mineral ligand-promoted

Deleted: , could be mainly present as

Deleted: organic

Deleted: complexes because of

Deleted: which implies a reductive ligand-promoted dissolution. Moreover, that study also confirms that OXL is the most effective ligand-promoting mineral-Fe solubility among organic binding ligands of Fe, due to its capacity as electron donor.

In the present study, we follow the recommendations of Johnson and Meskhidze (2013) based on the experiments by Paris et al. (2011) for OXL–promoted Fe dissolution of hematite, goethite and illite in cloud droplets and rainwater. Because the mineral database used for this study considers the average iron oxides (the goethite and hematite content) as a single iron oxide species (hematite), we take into account the fractional OXL-promoted Fe dissolution rates for hematite (α-Fe_2O_3) and goethite (α-$FeO(OH)$) proposed by Johnson and Meskhidze (2013), as presented in Table 3. The average values of relative proportions of Fe in the form of hematite and goethite to total iron oxide are based on experimental data for dust sources, compiled by Formenti et al. (2014), with their abundance in total iron oxide to be ~36% and ~64%, respectively.

Deleted: Hematite, Goethite
Deleted: Illite
Deleted: , the Hematite,
Deleted: Hematite
Deleted: Goethite
Deleted: from

DFe production during the organic ligand-promoted Fe dissolution is here considered to be in the form of Fe(II)-oxalato complexes in the aqueous-phase (i.e. in the ferrous oxidation state) and it is only applied to water droplets following the recommendations of the laboratory studies of Paris et al. (2011) and Paris and Desboeufs (2013). The aforementioned experiments have been performed with OXL concentrations found typically in rainwater and cloud droplets (0-8 μM), pH of 4.5 and dust concentrations of about 15 mg L^{-1}. Indeed, properties of the aqueous solution of clouds differ significantly to those of aerosols, with higher pH values (e.g. > 4), lower aqueous-phase dust concentrations (<50 mg L^{-1}) and lower ionic strength (Shi et al., 2012). On the other hand, the liquid aerosol content of typical continental aerosols can vary between $\sim 10^{-12}$ and 10^{-11} cm^3 cm^{-3} air, depending on the relative humidity, and the aerosol pH can vary between 1-4 (McNeill et al., 2012). Aqueous-phase OXL concentrations are significantly related to the transfer of small gas-phase polar compounds (e.g. glyoxal) to the liquid-phase (Carlton et al., 2007), a process that depends proportionally on the volume of the aqueous medium and on the pH of the solution. On the other hand, high acidic pH in the condense phase tends to favour the production of oligomeric structures rather than OXL (e.g. Lim et al., 2010; 2013). Thus, under such conditions of low aqueous-phase OXL concentrations, the ligand-promoted Fe dissolution may be suppressed significantly.

Deleted: For the present study, the
Deleted: Ferrus
Deleted: cloud
Deleted: Those
Deleted: 15mg/
Deleted: /
Deleted: 2013
Deleted: these low water-low pH

2.5 Aqueous-phase chemistry scheme

The global model simulates aqueous-phase chemistry in aerosol water and cloud droplets as described in Myriokefalitakis et al. (2011). To parameterize the Fe-speciation through the photochemical cycling of Fe(III)/Fe(II), the aqueous-phase chemical scheme has been further developed to account for the mineral-Fe dissolution processes and the ferric- and ferrous- oxalato complexes speciation (Fig. 1), taking into account recent global modelling studies (Johnson and Meskhidze, 2013; Lin et al., 2014 and references therein). Here, we use both the proton-promoted dissolution scheme as presented by Ito and Xu (2010) together with the ligand-promoted dissolution scheme as experimentally proposed by Paris et al. (2011). In Table S2 the updates in the chemical scheme of TM4-ECPL concerning Fe aqueous-phase chemistry that are adopted for the present study are listed. Fe aqueous-phase chemistry affects OXL net chemical production in two different ways: it reduces OXL by its oxidation to CO_2 (Ervens et al., 2003; Lin et al., 2014) during the rapid photolysis of ferrous-dioxalato complexes (Table S2), while it increases OXL production due to the enhancement in OH radical production via Fenton reaction (Table S2). These also affect modelled OXL concentrations that are re-evaluated in the supplementary Fig. S3 by comparison with observations compiled by Myriokefalitakis et al (2011).

Deleted: Ferric

Deleted: Ferrus

Deleted: chemistry that are adopted for the present study are listed.

2.6 Iron dissolution scheme

Johnson and Mekhidze (2013) have concluded that protons effectively promote Fe-containing minerals dissolution at rather acidic pH values (pH < ~2), while the OXL-promoted dissolution happens at higher pH values (pH > 3). To investigate the sensitivity of our chemical scheme to pH and OXL levels, we have performed box-model simulations to compare the iron solubility from our iron dissolution scheme in different acid and oxalate-load cases. The box-model calculations have been performed for dust concentrations 1 mg L^{-1}, pH values of 1.5, 4.5 and 8.5 and for initial oxalic acid concentrations of 0 μM, 4.5 μM and 8 μM. The percentage content of Fe in dust has been taken from Nickovic et al. (2013) as in the global TM4-ECPL model. Moreover, to take into account the Fe speciation due to aqueous-phase photochemical reactions, the box model also considers initial concentrations of $[H_2O_2] = 1$ μM, $[O_3] = 10^{-6}$ μM, $[OH] = 10^{-}$

Deleted: sensitivyt

Deleted: acidic

Deleted: environments

Deleted: and

Deleted: 5μM

Deleted: in

Deleted:]=

Deleted:]=

^{7} μM and $[HO_2] = 10^{-7}$ μM. Note that during the simulation pH values remains constant, but iron, oxalic acid as well as all other species concentrations change following the chemical scheme as described in Table S2. In Fig. S4, the SFe and the corresponding ferrous (SFe(II); SFe(II)=100*Fe(II)/TFe) and ferric (SFe(III); SFe(III)=100*Fe(III)/TFe) solubility fractions calculated for each simulation are presented.

According to our calculations after 10 days (240 hours of simulation), in the absence of OXL concentrations but in highly acidic pH values of 1.5, the SFe is calculated to reach ~10% (Fig. S4a), while at pH = 4.5 the SFe reached only ~0.2% in the form of Fe(II) (Fig. S4b) but at basic pH values of 8.5 the SFe was close to zero (Fig. S4c). In the presence of an initial OXL concentration of 4.5 μM, the box-model calculates no significant change of SFe for highly acidic pH of 1.5 (Fig. S4d) compared to the absence of OXL (since pH values remain constant during the simulation), while for pH=4.5 the SFe reached ~0.05% in the form of Fe(II) (Fig. S4e), and for pH=8.5 the SFe increased up to ~3.5% (also in the form of Fe(II)). This can be explained because in rather basic pH the mole fraction of oxalic acid ($pKa1 = 1.27$ and $pKa2 = 4.27$) is higher compared to acidic pH conditions and thus, the organic ligand-promoted dissolution tends to be more effective (Johnson and Meskhidze, 2013). In the case of high oxalic acid concentrations of 8 μM (Fig. S4g-i), the box-model calculates that Fe dissolution is effectively promoted by ligands. Indeed, for pH=8.5 and initial [OXL] = 8 μM (Fig. S4g), the box model calculates that SFe reaches ~6%. However, for pH=1.5 and [OXL] = 8 μM the SFe reaches also high values, although this can mainly be attributed to the proton-promoted dissolution since the mole fraction of oxalate is extremely low at these pH values. In contrast, for the case of a mid-range pH value (4.5), SFe reaches ~6% as a result of mainly ligand promoted dissolution (Fig. S4h) and to a lesser extend to the proton promoted one consistent with the no-OXL case as shown in Fig. S4b).

Although the aforementioned sensitivity box-modeling studies show the significance between the proton- and ligand- promoted Fe dissolution depending on the chemical conditions, the proton-promoted dissolution is expected to be more important under atmospheric conditions. While high basic pH values are associated with dust alkalinity

Deleted: S9
Deleted: after 10 days
Deleted: by
Deleted: of our box-model simulations
Deleted: ,
Deleted: S9a
Deleted: is reaching
Deleted: 1% and
Deleted: highly
Deleted: barely reaches 0.03%.
Deleted: 5μM
Deleted: at the same pH,
Deleted: reaches ~4%
Deleted: is raised
Deleted: 7%.
Deleted: highly
Deleted: values
Deleted: fractions
Deleted: oxalate are
Deleted: less basic and strong
Deleted: values
Deleted: less
Deleted: , as already noted by
Deleted: (
Deleted: S9
Deleted: the more
Deleted: than by protons.
Deleted:]=8μM
Deleted: S9b
Deleted: 10% as in the case of highly acidic pH in the absence of OXL (Fig S9a).
Deleted:]=8μM
Deleted: that
Deleted: only
Deleted: in
Deleted: 7
Deleted: (Fig S9b, Fig S9a).
Deleted: alteration
Deleted: in the
Deleted: only

(Ito and Feng, 2010) located close to dust sources, no significant oxalic acid sources, which are controlled mainly from biogenic NMVOC emissions and cloudiness (Myriokefalitakis et al., 2011), are expected to be found near the desert regions (e.g. the Sahara).

3 Results and Discussion

3.1 Primary and secondary sources of dissolved iron

In Fig. 2, the annual mean primary DFe emissions from fossil fuel combustion processes (including oil combustion from ships) (Fig. 2a), biomass burning (Fig. 2b) and from Fe-containing minerals (Fig. 2c) sources are shown together with the annual mean total mineral Fe-dissolution flux (sum of proton- and organic ligand- promoted Fe dissolution fluxes; secondary DFe sources) as calculated by the model (Fig. 2d). The model takes into account ~0.070 Tg-Fe yr^{-1} of DFe anthropogenic emissions with most of them occurring over densely populated regions of the globe (the mid-latitudes of the northern hemisphere, e.g. China, Europe and the US; ~0.1-1 ng-Fe m^{-2} s^{-1}), but also in the remote oceans (e.g. Northern Atlantic Ocean, Northern Pacific Ocean), due to oil-combustion processes downwind of shipping lanes (up to 0.05 ng-Fe m^{-2} s^{-1}). Primary emissions of DFe from biomass burning (Fig. 2b) peak over tropical forested areas (~1 ng-Fe m^{-2} s^{-1}) and according to model calculations, biomass burning contributes about ~0.127 Tg-Fe yr^{-1}, showing maxima over Central Africa and Amazonia during the dry season. DFe emissions associated with mineral dust (Fig. 2c) of ~0.125 Tg-Fe yr^{-1}, are emitted mainly over the Saharan desert region however, important emissions are also found over other desert areas of the globe (e.g. the Gobi Desert, Middle East and Australia).

Deleted: anthropogenic

Deleted: contacting

Deleted: 071

Deleted: to occur

Deleted: the

Deleted: .

Deleted: in contrast to those from anthropogenic activities that peak over the mid-latitudes of the northern hemisphere. According

Deleted: 128

Deleted: but

The secondary sources of DFe in the atmosphere result from both the proton- and ligand-promoted dissolution processes of Fe-containing mineral in the model (Fig. 2d). The total annual mineral Fe-dissolution flux is calculated to be ~0.175 Tg-Fe yr^{-1} of DFe by TM4-ECPL. As shown in Fig. 2d, most of the dissolution occurs downwind of the dust source region, where long- and regional- range transport of natural and anthropogenic pollution

Deleted: 163

sources enhance the release of DFe from the minerals. Thus, the model calculates maximum dissolution fluxes over the Persian Gulf, downwind of the Sahara and Beijing, downwind the Gobi Desert (~1 ng-Fe m^{-2} s^{-1}). However, enhanced mineral-Fe dissolution fluxes (~0.1 ng-Fe m^{-2} s^{-1}) are calculated over the whole area of the Middle East, the Eastern Mediterranean basin, as well as over the remote oceans like the tropical Atlantic Ocean, and India and the outflow of Asia to the Pacific Ocean.

3.2 Proton- versus organic ligand-promoted mineral iron mobilisation

The proton- and the organic ligand- promoted dissolution of Fe-containing minerals are compared in Fig. 3a and 3b respectively. According to TM4-ECPL calculations on a global scale, almost 80% of dust Fe dissolution occurs through proton-promoted dissolution (Fig. 3a; ~0.137 Tg-Fe yr^{-1}), where high proton concentrations destabilize Fe-oxygen (Fe-O) bonds in the crystal lattice of the Fe-containing minerals. Proton-promoted Fe dissolution dominates downwind of dust source areas and heavy population regions (e.g. Beijing; ~1.00 ng-Fe m^{-2} s^{-1}) where atmospheric acidity is high due to SO_x and NO_x anthropogenic emissions. On the other hand, because of long-range transport, relatively high rates of organic ligand-promoted dissolution (~0.1 ng-Fe m^{-2} s^{-1}) are calculated over Central Africa, Amazonia and the equatorial Atlantic Ocean (Fig. 3b), where biogenic NMVOC oxidation and cloudiness lead to enhanced OXL aqueous-phase formation (Myriokefalitakis et al., 2011).

3.3 Iron concentrations

The calculated global annual mean TFe and DFe atmospheric surface distributions are shown in Fig. 4a and Fig. 4b (note differences in scales), respectively (the dissolved Fe(III) and Fe(II) in Fig. S5a-b and S5c-d in the Supplement, respectively), and the fractions of Fe(II) to DFe are presented in Fig. 4c. Maxima annual mean concentrations of more than 100 μg-Fe m^{-3} are calculated to occur over the Sahara and Gobi deserts near the surface (Fig. 4a). However, the outflow from these source regions transports TFe over the global ocean, with the highest impact to be calculated for the Northern Hemisphere (Fig. 4a). The DFe concentrations (sum of Fe(III) and Fe(II)) are calculated to be about

Deleted: like the

Deleted: the Gobi desert,

Deleted: the Middle East

Deleted: *Fe*

Deleted: ~

Deleted: of Fe

Deleted: 129

Deleted: mineral

Deleted: to

Deleted: close to

Deleted: (Fig. 3b

Deleted: (close to 0.05 ng-Fe m^{-2} s^{-1}

Deleted: high

Deleted: *Fe Concentrations*

Deleted: ,

Deleted: ,

Deleted: S2a

Deleted: S2c

Deleted: ,

Deleted: 4c (note differences in scales).

Deleted: air

Moved (insertion) [5]

Deleted: . The

Moved up [5]: 4a).

Deleted: African Fe sources also affect the middle troposphere through atmospheric transport along the tropical Hadley cell. ¶

three orders of magnitude lower than the TFe (Fig. 4b). As for TFe, the outflow from the continental source regions is clearly seen in the calculated DFe distributions. The enhanced concentrations of Fe (III) over polluted regions, determine the importance of atmospheric acidity and anthropogenic DFe emissions (Fig. S5a). Over Central South America, Asia and Indonesia, high concentrations of DFe (~50-100 ng-Fe m^{-3}) are calculated both due to biomass burning DFe emissions but also due to organic ligand-promoted dissolution, which is enhanced in these areas by the OXL produced from oxidation of emitted biogenic NMVOCs via clouds.

African Fe sources also affect the middle tropospheric DFe concentrations through atmospheric transport along the tropical Hadley cell. Model calculations show that Fe(III) (Fig. S5b) and Fe(II) (Fig. S5d) have significant concentrations in the middle troposphere owing to transport from the source regions. Note, however, that in-cloud and in aerosol water aqueous phase chemical processing transforms also a significant part of TFe to DFe in the upper troposphere.

Model calculations also demonstrate the importance of photochemical redox cycling of Fe(III)/Fe(II) in the aqueous-phase (aerosols and clouds) of the atmosphere. Fig. 4c shows the percentage contribution of Fe(II) to DFe as computed by the model, denoting that the calculated Fe(II) concentrations are an important part of DFe atmospheric burden; regionally reaching up to 20% of the total dissolved mass far from the dust source areas e.g. the remote ocean. This ratio also exceeds 10% at several other locations around the globe, in particular over the tropical Pacific and the Southern Ocean; implying that chemical aging of dust due to atmospheric processing and long-range transport enhances significantly the production of Fe(II). As also discussed in Sec. 2.6, in relatively basic pH environments (e.g. the Southern Ocean due to the buffering capacity of sea-salt particles; see Fig. S2a,b) and due to high OXL concentrations (e.g. tropical Pacific ocean) the production of Fe(II) is favoured (Fig. S4e and Fig. S4h, respectively). Thus, our model calculations indicate that the enhanced fraction of Fe(II) over the remote oceans (Fig. 4c), characterized by low concentrations of dust and non-negligible OXL concentrations (see Fig. S3) due to the aqueous-phase oxidation of organic compounds of

Deleted: S2a and S2c

Moved down [6]: the remote ocean.

Deleted: Model calculations also demonstrate the importance of photochemical redox cycling of Fe(III)/Fe(II) in the aqueous phase (aerosols and clouds) of the atmosphere. Figures S2c and S2d denote that calculated Fe(II) concentrations are an important part of DFe atmospheric burden, regionally reaching up to 50% of the total dissolved mass far from the dust source areas e.g.

Deleted: dust

Deleted: such as Mexico (~40 ng-Fe m^{-3})

Deleted: S2a

Deleted: Fe(III) (Fig. S2b) and Fe(II) (Fig. S2d) show significant concentrations in the middle troposphere owing to transport from the source regions but also from in-cloud and in aerosol water chemical processing that transforms part of TFe to DFe in the atmosphere. Fig. 4c shows the percentage contribution of Fe(II) to DFe as computed by the model for the surface and the zonal mean distribution. This ratio exceeds ~10% at several locations around the globe in particular over remote oceanic regions, as for instance in the tropical Pacific and the tropical North Atlantic Ocean. This implies that chemical aging of dust due to long-range transport enhances significantly the Fe(II) production.

Moved (insertion) [6]

marine origin NMVOCs (e.g. isoprene) could be attributed to the production of ferrous-oxalato complexes.

TM4-ECPL calculates a global TFe atmospheric burden of ~0.857 Tg-Fe and almost 35 times lower atmospheric burden of the DFe ~0.024 Tg-Fe (~0.023 Tg-Fe as Fe(III) and ~0.001 Tg-Fe as Fe(II)). This also indicates the existence of a large TFe reservoir that can be mobilized under favourable conditions. The total SFe (Fig. S6a) is calculated to vary spatially with minima over the dust sources (~1%) and maxima over the south equatorial regions (~5%). SFe due to dust aerosols is attributed primarily to the atmospheric processing and to the (low) initial dust solubility. These low SFe values over dust source regions can be also explained by the suppressed mineral Fe-dissolution because of the enhanced buffering capacity (as well as the low water associated with dust aerosols near their sources), the low acidity because of the low amounts of acidic inorganic compounds from anthropogenic pollution and the lack of organic ligands (e.g. OXL) over large dust outbreaks (e.g. the Sahara) (Fig. S6b). On the other hand, the model calculates higher SFe values (~2.5-5%) of dust aerosols over regions characterized by low dust concentrations but high amounts of anthropogenic pollution (e.g. over the Indian Ocean). However, the co-existence of relatively high dust concentrations and high amounts of anthropogenic pollutants tends to enhance significantly Fe-mineral atmospheric processing and thus SFe (~5%), as in the case of the Persian Gulf and Eastern Mediterranean (Fig. S6b). Fe-containing combustion aerosols of anthropogenic origin (Fig. S6c) are also calculated to contribute significantly to SFe (~2.5%) over high population regions (e.g. the US, central Europe and China). Due to the long-range transport in the Northern Hemisphere, enhanced SFe is simulated also over the Northern Atlantic and Pacific Oceans (~1.5%). Additionally, biomass burning processes are calculated to increase SFe, especially over the Southern Hemisphere. The atmospheric transport of dissolved Fe containing combustion aerosols from the Central Africa, Amazonia and Indonesia over the Southern Pacific, Atlantic and Indian Oceans (from the equator to ~50S) is found to increase significantly the SFe (~5%). Overall, model calculations denote that from the computed global average SFe of about 2.8%, 1.3% comes from dust, 1.2% from biomass burning aerosols and 0.3% from fossil fuel combustion processes. The average lifetime of TFe is

Deleted: 454

Deleted: 40

Deleted: 012

Deleted: 011

Deleted: This implies an overall fractional solubility for atmospheric Fe of ~2.6% and

Deleted: (τ_{TFe})

calculated to be about 5 days while that of DFe is found to be longer (~6 days on average) due to DFe association with atmospheric aerosol that has been transported and processed in the atmosphere and thus resides overall in smaller size aerosols than TFe. In our model, DFe resides mostly in small particles (~ 60%) and thus is more effectively transported in the atmosphere reaching the global ocean compared to the bulk TFe mass that is carried mainly by coarse aerosols (~80%).

3.4 Model iron concentration evaluation

Observations of total and dissolved Fe concentrations in ambient aerosols near the surface are valuable to evaluate our understanding of the Fe cycle as parameterized in the models. TM4-ECPL daily mean results are here validated against daily observations of total (Fig. 5a) and dissolved Fe (Fig. 5b) associated with atmospheric aerosols over the Atlantic Ocean (Baker et al., 2013) and the Indian Ocean (Witt et al., 2006) as compiled by Sholkovitz et al. (2013). Figure 5c also presents the comparison of daily solubility fractions of the above observations versus the respective calculated fractions by the model. In addition, Fe aerosol data compiled by Mahowald et al. (2005) are compared with model results in Fig. 5d. The seasonality of TFe in the Eastern Mediterranean as measured and compiled by Koulouri et al. (2008) at Finokalia station (http://finokalia.chemistry.uoc.gr/) is also compared to monthly model results (Fig. 5e).

The comparisons presented in Fig. 5 show that the model reasonably simulates the observed concentration of total and dissolved Fe in the ambient aerosols over oceans (scatter plots in Fig. 5a, 5b and 5c). In the East Mediterranean, when comparing to ambient aerosol observations at Finokalia monitoring station (Fig. 5e), the model seems to underestimate the observations of TFe with the largest differences calculated for January-February, May and July-September. These are the periods of the year that Finokalia station can be occasionally affected by strong dust outbreaks from Africa (Kalivitis et al., 2007) that are better represented in the observations than in the model results due to their episodic character. All evaluations (see supplementary material Table S3) are based on statistical parameters of correlation coefficient (R; Eq. S1), normalised

Deleted: (τ_{DFe})

Deleted: its

Deleted: residing

Deleted: than

Deleted: *Fe*

Deleted: 2012

Deleted: (2013).

Deleted: Mahowland

Moved (insertion) [7]

Deleted: 5c. All evaluations (see supplementary material Table S3) are based on statistical parameters of correlation coefficient (R; eq. S1), normalised mean bias (NMB; eq. S2), root mean square error (RMSE; eq. S3), and normalised mean error (NME; eq. S3). ¶

Deleted: East

Deleted: Theodosi

Deleted: 2010

Deleted: as shown in

Moved up [7]: 5d.

Formatted: Space Before: 12 pt, Line spacing: 1.5 lines

Deleted: Theodosi et al., 2010) (Fig 4d

Deleted: Jan-Feb

Deleted: Sept

mean bias (NMB; Eq. S2), root mean square error (RMSE; Eq. S3), and normalised mean error (NME; Eq. S3).

3.5 Iron deposition

TM4-ECPL calculates that ~37 Tg-Fe yr^{-1} of TFe are deposited to the Earth's surface (Fig. 6a). The highest annual deposition fluxes of TFe of ~100 ng-Fe m^{-2} s^{-1} (i.e. ~3.2 g-Fe m^{-2} yr^{-1}) are calculated to occur over the Sahara and Gobi deserts. Significant deposition fluxes up to ~10 ng-Fe m^{-2} s^{-1} are also calculated at the outflow from these source regions over the Atlantic and Pacific Oceans. The computed global DFe deposition is ~0.496 Tg-Fe yr^{-1} of which ~0.191 Tg-Fe yr^{-1} is deposited over the ocean (Fig. 6b). This oceanic DFe deposition estimate is lower than an earlier reported DFe deposition flux to the ocean of 0.26 Tg-Fe yr^{-1} (Johnson and Meskhidze, 2013). However, that study used dust emissions of ~1900 Tg yr^{-1}, about 60% larger than the dust sources in the present study (~1091 Tg yr^{-1} for the year 2008). In addition, at least a 50% of uncertainty in the calculated deposition fluxes was found to be associated with the applied horizontal resolution of the model, with higher fluxes calculated by the higher model resolution.

Figures 6c-6f present the seasonal variability of DFe deposition as calculated by TM4-ECPL (in parenthesis the deposition fluxes over the oceans are also provided). The maximum global seasonal DFe deposition flux of ~0.132 Tg-Fe season^{-1} is calculated to occur during JJA (June-July-August; Fig. 6e), followed by fluxes of ~0.128 Tg-Fe season^{-1} during DJF (December-January-February; Fig. 6c) and ~0.127 Tg-Fe season^{-1} during MAM (March-April-May; Fig. 6d). The enhanced photochemistry during summertime over the Northern Hemisphere increases the atmospheric acidity due to NO$_x$ and SO$_x$ oxidation, and thus enhances proton-dissolution of mineral dust. However, combustion emissions from biomass burning and oil combustion of anthropogenic origin also contribute significantly to the DFe tropospheric concentrations. Moreover, OXL aqueous-phase formation and therefore organic ligand-promoted Fe dissolution is favoured due to the high biogenic NMVOC emissions during the warm season (Myriokefalitakis et al., 2011). On the contrary, during SON (September-October-

Deleted: *Fe Deposition*

Deleted: 34

Deleted: near the surface.

Deleted: , with the highest outflow impact calculated for the Northern Hemisphere

Deleted: outflows of

Deleted: calculated to be

Deleted: 489

Deleted: 124

Deleted: global

Deleted: to

Deleted: global oceanic

Deleted: according to

Deleted: (2014

Deleted: that is

Deleted: ~

Deleted: that

Deleted: the TM4-ECPL takes into account for this work (~1088

Deleted: .

Deleted: 136

Deleted: the flux

Deleted: During the aforementioned periods, the

Deleted: atmospherically-driven

Deleted: enhanced

November; Fig. 6f) the model calculates lower DFe deposition fluxes, of ~0.109 Tg-Fe season^{-1} due to the weaker photochemical activity and therefore the lower Fe dissolution fluxes both from proton- and organic ligand- promoted dissolution. Note, also, that most dust and TFe emissions occur in the mid-latitudes of the Northern Hemisphere where the majority of anthropogenic emissions of acidity precursors also occur (Fig. S1).

3.6 Model iron deposition evaluation

In Fig. 7, TM4-ECPL deposition fluxes of TFe and DFe (this work) are compared to the estimates over four Atlantic Ocean regions (Fig. S7a-d) based on the observations of Baker et al. (2013) as well as the deposition fields from the modelling studies of Mahowald et al. (2009) and Johnson et al. (2010) as compiled and presented by Baker et al. (2013). Both of these modelling studies assumed a constant Fe content of 3.5% in dust and a proton-promoted Fe dissolution. DFe deposition fluxes have been calculated for 4 regions as described in Baker et al. (2013), with Region 2 corresponding to North Atlantic dry regions, Region 3 corresponding to intertropical convergence zone (ITCZ), Region 4 to South Atlantic dry regions and Region 5 to South Atlantic storm rainfall (Fig. S7a-d).

In the South Atlantic (Region 4) during AMJ (April-May-June) TM4-ECPL calculations of TFe deposition show a broad agreement with the measurements and also agree with the other modelling studies, when taking into account the large uncertainty associated with these estimates. On the other hand, the model overestimates the measurements of TFe in Region 2 and Region 3 during AMJ, similarly to the modelling study by Mahowald et al. (2009). These regions are both strongly affected by Sahara dust outflow. Thus the model overestimate of TFe observations by Baker et al. (2013), while DFe observations are much better captured by the model, could be due to a longer lifetime of TFe in the model than in the atmosphere resulting from smaller size distributions of TFe in the model than in reality. During SON (Fig. 7b), TM4-ECPL overestimates the measured values from Baker et al. (2013), similarly to the modelling study by Mahowald et al. (2009). For Region 4 during SON the model agrees well with the Baker et al. (2013) estimates and calculates lower TFe deposition fluxes compared to Mahowald et al. (2009)

Deleted: 6f) and DJF (December-January-February; Fig. 6c),

Deleted: 104 Tg-Fe and ~0.122

Deleted: , respectively,

Deleted: slower

Deleted: of

Deleted: are occurring

Deleted: are occurring

Deleted: *Fe*

Deleted: S10

Deleted: in

Formatted: Space Before: 12 pt, Line spacing: 1.5 lines

Deleted: the dry season

Deleted: the

Deleted: the wet season (September-October-November –

but very close to the estimation from Johnson et al. (2010). Overall, TM4-ECPL model overestimates the observed DFe deposition over Regions 2, 3 and 4 during both studied periods, while it underestimates DFe deposition over Region 5, similarly to other model estimates (Fig. 7c,d).

4 Sensitivity of dissolved iron to air-pollutants

Deleted: **Dissolved Iron**

Deleted: **Air Pollutants**

The response of mineral-Fe dissolution to the changes in emissions is here assessed by comparing simulations performed using anthropogenic and biomass burning PAST and FUTURE emissions (see Sect. 2). Atmospheric acidity strongly depends on SO_x and NO_x anthropogenic emissions and Fe solubility is impacted by atmospheric acidity as discussed above. Minerals dissolution is therefore expected to be significantly affected by anthropogenic emissions. Iron anthropogenic and biomass burning emissions also vary as shown in Table 1 and explained in Sect. 2.3. Note, however, that meteorology, dust emissions and biogenic NMVOC emissions (and thus OXL precursors from biogenic sources) are kept constant for both PAST and FUTURE simulations, corresponding to the year 2008 (i.e. PRESENT simulation). Thus, the computed changes for species that regulate the mineral-Fe proton- and ligand-dissolution (e.g. SO_4^{2-}, NH_4^+, NO_3^- and OXL), as presented in Fig. S8, are due to the respective anthropogenic and biomass burning emission differences between PAST, PRESENT and FUTURE simulations.

Deleted: section

Deleted: section

Deleted: VOC

Deleted: formation

Deleted: fig. 8.

Deleted: only

Deleted: changes

4.1 Past and future changes in iron dissolution

Deleted: *Future*

Deleted: *Fe*

For the PAST simulation, the anthropogenic emissions (e.g. NO_x, NH_x and SO_x) are a factor of 5-10 lower than present day emissions (Lamarque et al., 2010). Thus, compared to the present day, the model calculates significant changes in the aerosol-phase pH in the PAST simulation with less acidic (aerosol and cloud) pH over the surface Northern Hemisphere oceans but a more acidic pH, over Europe due to extensive coal combustion in 1850 (Fig. S2e,g,i). FUTURE simulation projects in general a less acidic aerosol pH (Fig. S2f,h,j) when compared to the present-day simulation, owing to lower NO_x and SO_x emissions. Indeed, for the FUTURE simulation, anthropogenic emissions for most of the

Deleted: S4a

Deleted: S4b

continental areas are projected to be lower than the present-day and to almost return to pre-1980 levels due to air quality regulations (Lamarque et al., 2013).

Past and future changes of the atmospheric acidity (Fig. S2) have a significant effect on mineral-Fe dissolution (Fig. 8a and Fig. 8b respectively). For the PAST simulation the model calculates about 80% lower proton-promoted mineral Fe dissolution (~0.025 Tg-Fe yr^{-1}) compared to PRESENT simulation (~0.137 yr^{-1}). As far as the FUTURE simulation is concerned, proton-promoted mineral Fe dissolution (~0.036 Tg-Fe yr^{-1}) is also projected to be about three times lower than at present. In contrast to these changes due to atmospheric acidity, higher contribution of organic-ligand to the total mineral-Fe dissolution is computed; for the PAST and FUTURE simulations the model calculates higher global-scale organic ligand-promoted mineral Fe dissolution (~0.040 Tg-Fe yr^{-1} and ~0.045 Tg-Fe yr^{-1}, respectively) compared to the PRESENT (~0.038 yr^{-1}). Thus, the contribution of organic ligand-promoted mineral-Fe dissolution process to the total dissolution flux is calculated to show an inverse pattern compared to the proton-promoted one (Fig. 8c,d). Differences in the pH of atmospheric (aerosol and cloud) water and oxidant levels can affect significantly OXL aqueous-phase chemical production (Myriokefalitakis et al., 2011). According to TM4-ECPL calculations the increase in OXL levels enhances the organic-ligand promoted Fe-mineral dissolution in remote oceanic regions with very low dust load. However, dust load over the remote oceans could increase if dust outbreaks become more important in the future (Goudie, 2009). One other aspect of the organic ligand-promoted mineral-Fe dissolution is also the effect on the speciation of dissolved and bioavalable Fe. According to the chemical scheme used in this work, the production of Fe(II)-oxalato complexes increases significantly the ferrous content in the DFe, in contrast to the proton-promoted mineral-Fe dissolution where Fe(III)-complexes dominate total DFe production. Indeed, when only the proton-promoted Fe dissolution is considered in our model, the ferrous-complexes are produced during the day, when the Fe(III) is converted into Fe(II) as a result of the Fe(III) photolysis (e.g. Deguillaume et al., 2004). However, when the organic ligand Fe-dissolution is taken into account, the Fe(II) is increased, since there is production of ferrous complexes even under dark conditions. This may explain also the observed high

Deleted: three-times

Deleted: 041

Deleted: the

Deleted: 129

Deleted:) (Fig. 8a

Deleted: 039

Deleted: (Fig. 8b). ¶

Deleted: parallel

Deleted: the aforementioned computed differences

Deleted: changes in the

Deleted: are also computed. The

Deleted: is calculated

Deleted: gain importance for

Deleted: (Fig. 8c,d), showing

Deleted: can enhance significantly

Deleted: of

Deleted: Ferrus

Deleted: Ferrus

Deleted: as also the

Deleted: . (

Deleted:) proposed.

Deleted: Ferrus-

Deleted: without sunlight.

Deleted: can

Fe(II) content compared to Fe(III) in the DFe in precipitation over the Mediterranean (Theodosi et al., 2010). However, our model calculates much lower Fe(II) content in DFe (Fig. 4c) compared to that study indicating a model underestimate of Fe(II) source potentially those associated with the organic ligand promoted contribution to DFe. TM4-ECPL calculates that the decrease in the atmospheric acidity both in the PAST and in the FUTURE compared to the PRESENT simulations increases the importance of organic-ligand mineral-Fe dissolution and thus leads to a significant enhancement of the Fe(II) surface concentrations and thus its content in DFe (Fig. S9 a,b) and a simultaneous reduction of Fe(III) (Fig. S9 c,d).

4.2 Past and future changes in iron deposition

The model calculates a DFe deposition flux of ~0.213 Tg-Fe yr^{-1} (with ~0.063 Tg-Fe yr^{-1} over oceans) in the PAST that is about half (to one third over the oceans) (Fig. S9e, negative differences) compared to PRESENT (~0.496 Tg-Fe yr^{-1} with ~0.191 Tg-Fe yr^{-1} over oceans). On the other hand, FUTURE DFe deposition is calculated to be ~0.369 Tg-Fe yr^{-1} (with ~0.136 Tg-Fe yr^{-1} over oceans) which is about 25% lower than the simulated global PRESENT deposition (Fig. S9f). This can be explained by lower amounts of combustion DFe-containing aerosols simulated to be emitted in the PAST (~0.011 Tg-Fe yr^{-1} from fossil fuel combustion and ~0.013 Tg-Fe yr^{-1} from biomass burning aerosols) compared to the PRESENT simulation (~0.070 Tg-Fe yr^{-1} from fossil fuel combustion and ~0.127 Tg-Fe yr^{-1} from biomass burning aerosols), as well as in the FUTURE (~0.013 Tg-Fe yr^{-1} from fossil fuel combustion) compared to the PRESENT simulation. However, higher emissions of biomass burning Fe-containing aerosols are projected for the FUTURE (~0.155 Tg-Fe yr$^{-1)}$ that (see also Table 1) that counteract the projected lower Fe emissions contained in fossil fuel aerosols and the weaker mineral Fe-dissolution for the FUTURE simulation. The weaker acidification of mineral dust in the PAST and FUTURE compared to the PRESENT atmosphere (Fig. S7e,g,i and Fig. S7f,h,j respectively) can be also seen in SO_4^{2-} and NO_3^- surface concentrations, by the negative changes from present day shown in Fig. S8a,c and Fig. S8b,d, respectively.

Deleted: 2010). The relative contribution of these two types of dissolution can be also seen by the percentage differences of PAST and FUTURE ferric and ferrous fractions, respectively, in the calculated DFe (Fig. S7).

Deleted: S7

Deleted: S7c;

Deleted: *Future*

Deleted: *Fe*

Deleted: 230

Deleted: 050

Deleted: lower

Deleted: S8a

Deleted: 489

Deleted: 124

Deleted: Differences are also apparent for the SFe (Fig. S8c), with by up to ~80% lower values in

Deleted: PAST compared to PRESENT over the global oceans as well as over highly populated regions of the world. This can be explained by the weaker acidification of mineral dust in the PAST than in the PRESENT atmosphere (also shown by the negative changes from present day in SO_4^{2-} and NO_3^- surface concentrations in Fig. S3a,c). Note, however, that significantly lower amounts of combustion aerosols Fe are simulated to be emitted in the PAST simulation (see Table 1).

Deleted: 372

Deleted: 088

Deleted: 8f). The reduction in SFe

Deleted: present day (Fig. S8d) is calculated to be up to ~70% over the mid-latitudes of the Northern Hemisphere and up to 50% over the southern hemisphere

Deleted: tropical-subtropical oceanic regions.

4.3 Biogeochemical implications

The determination of iron solubility is important to understand the carbon biogeochemical cycle. Okin et al. (2011) have shown that in HNLC areas, atmospheric deposition of Fe to the surface ocean could account for about 50% of carbon fixation, although they pointed to the large uncertainties in the speciation and solubility of deposited Fe that are associated with these estimates. Thus, the impact of Fe on ocean productivity, and subsequently on Earth's climate system, is expected to be most important in HNLC areas such as the Southern Ocean (Boyd et al., 2000). However, because the DFe deposited from the atmosphere to the surface water follows the water flow inside the ocean, atmospheric deposition impact is expected to be geographically extended compared to the surfaces where this deposition occurs and can be only evaluated by an ocean biogeochemical model. For the characterization of HNLC oceanic regions in this study, the annual mean global NO_3^- surface water concentrations from the LEVITUS94 World Ocean Atlas (http://iridl.ldeo.columbia.edu/SOURCES/.LEVITUS94/) and the monthly chlorophyll-a (Chl-a) concentrations MODIS retrievals taken into account in the model (Myriokefalitakis et al., 2010) for the year 2008 are used. The model grid boxes corresponding to HNLC waters (Fig. S7e) are here defined based on the co-occurrence of surface seawater NO_3^- concentrations of > 4 µM (Duce et al., 2008) and Chl-a concentrations of < 0.1 mg m^{-3} (Boyd et al., 2007).

The deposition fluxes of TFe and DFe over oceans are presented in Fig. 9a and Fig. 9b, respectively. The model calculates that ~1.052 Tg-Fe yr^{-1} of TFe are deposited over the HNLC ocean with the maximum deposition fluxes calculated over the Northern Pacific Ocean (~5-10 ng-Fe m^{-2} s^{-1}) and the lowest over the Southern Ocean (~0.05-0.5 ng-Fe m^{-2} s^{-1}). The same pattern is also calculated for the DFe deposition, with maximum DFe deposition fluxes over the equatorial Atlantic Ocean (~0.5 ng-Fe m^{-2} s^{-1}), relatively high deposition fluxes over the Northern Pacific Ocean (~0.01-0.05 ng-Fe m^{-2} s^{-1}) and lower over the Southern Ocean (up to ~0.005 ng-Fe m^{-2} s^{-1}). TM4-ECPL calculates a deposition flux of ~ 0.033 Tg-Fe yr^{-1} of DFe over the HNLC waters which represents ~17% of the total oceanic DFe deposition flux and ~7% of the global one.

Deleted: *Implications*

Formatted: Font: Bold, Not Italic

Formatted: Font: Bold, Not Italic

Deleted: However,

Deleted: order

Deleted: estimate

Deleted: the

Deleted: thus on the impact

Deleted: the study of DFe deposition has to

Deleted: focused of the

Deleted: waters

Deleted:), since

Deleted: current major dust

Deleted: oceanic regions (e.g. the Atlantic Ocean downwind to Sahara) are already dust-Fe saturated and no significant

Deleted: implications are expected due to changes in Fe dissolution there. Thus, for the present study the differences on Fe deposition are also calculated for the HNLC water where Fe is expected to limit the primary productivity.

Deleted: in use

Deleted: mM

Deleted: HNLC waters

Deleted: 0.478

Deleted: to be

Deleted: higher

Deleted: (~

Deleted: 021

Deleted: but only ~4

The percentage differences of calculated PRESENT DFe deposition fluxes over oceans from the PAST and FUTURE simulations are depicted in Fig. 9c and 9d, respectively. The model in general calculates for both PAST and FUTURE simulations lower DFe deposition fluxes over oceans. DFe deposition fluxes are calculated to be ~80% higher in the PRESENT than in the PAST simulation (Fig. 9c), which can be attributed both to the increase of i) mineral Fe dissolution (almost 3-fold) and ii) primary DFe emission (from both fossil fuel combustion (6-fold) and biomass burning sources (almost an order of magnitude)). Furthermore, based on emission projections following air quality legislation, decreases of about 30-60% in DFe deposition are calculated for the FUTURE simulation over the Northern Pacific and Atlantic oceans, the Arabian Sea, the Bay of Bengal and the East Mediterranean Sea and lower reductions (less than 20%) over the remote tropical Pacific and Atlantic Oceans and the Southern Ocean. These smaller changes from the PRESENT simulation calculated for the FUTURE (globally about 45% reduction) than for the PAST (globally almost 3-fold change) are attributed to the projected increase of Fe biomass burning emissions (about 20%) that partially counterbalance the more than 5-fold reduction in anthropogenic emissions of Fe. Overall, these sensitivity PAST-to-FUTURE simulations clearly support that changes in i) atmospheric acidity and ii) Fe combustion sources, both driven by anthropogenic pollutants emissions, affect significantly DFe deposition over the oceans, and therefore they have the potential to also perturb open-ocean phytoplankton growth and thus the carbon biogeochemical cycling.

5 Conclusions

Primary Fe emissions from dust and combustion sources (fossil fuel and biomass burning) of TFe and DFe, as well as the atmospheric processing by proton- and organic ligand- promoted mineral Fe-dissolution together with aqueous-phase photochemical reactions between oxidation states of Fe (III/II), are taken into account in the state-of-the-art chemistry transport model TM4-ECPL. The model calculates for present day conditions an atmospheric Fe dissolution flux of ~0.175 Tg-Fe yr^{-1} of which ~22% is

Deleted: over the HNLC oceans

Deleted: simulation

Deleted: the HNLC waters. An increase of ~50% is

Deleted: have happened

Deleted: latest 150 years (

Deleted: versus PRESENT

Deleted: ,

Deleted:)

Deleted: the increase of

Deleted: (to a lesser extent) the increase of

Deleted: anthropogenic

Deleted: significant

Deleted: over the HNLC oceans

Deleted: , although with smaller changes than those computed for the PAST simulation. The decrease in mineral Fe dissolution due to air-quality legislations projected for the future atmosphere leads to a reduction of DFe deposition of ~30%

Deleted: HNLC oceanic regions (i.e. North

Deleted: North

Deleted:)

Deleted: ~

Deleted: %

Deleted: Ocean and the Southern Ocean. The

Deleted: PRESENT

Deleted: the

Deleted: HNLC waters

Deleted: blooms

Deleted: dust

Deleted: (minerals)

Deleted: anthropogenic and biomass-burning (

Deleted:)

Deleted: and

Deleted: different forms

Deleted:)

Deleted: accounted for

Deleted: 163

Deleted: 20

attributed to the impact of organic ligands on the Fe cycle. The atmospheric burden of DFe is calculated to be ~0.024 Tg-Fe and the dissolved Fe annual deposition flux over the oceans to be ~0.119 Tg-Fe yr^{-1}. SFe (global mean of about 2.8%) is calculated to vary spatially with minima over the dust sources (~1%). This global mean solubility of Fe, originates from dust (1.3%), biomass burning aerosols (1.3%) and fossil fuel combustion (0.3%). Note that these model estimates are associated with large uncertainties in the kinetics of Fe dissolution as well as the primary total and dissolved Fe emissions. As earlier explained, model results depend on model resolution but more importantly depend on assumptions made in the model, such as neglecting any organic ligand dissolution of Fe in aerosol water and treating biomass burning and fossil fuel burning DFe as primary.

Sensitivity simulations show that increases in anthropogenic and biomass burning emissions since 1850 resulted in both enhanced Fe combustion emissions and a more acidic environment and thus more than double DFe deposition (~0.213 Tg-Fe yr^{-1} in the year 1850 against ~0.496 Tg-Fe yr^{-1} nowadays). Air-quality regulations are projected to decrease anthropogenic emissions and thus atmospheric acidity in 2100. Our model results show a 5-fold decrease in Fe emissions from anthropogenic combustion sources (~0.013 Tg-Fe yr^{-1} in the year 2100 against ~0.070 Tg-Fe yr^{-1} nowadays), and about 45% reduction in mineral Fe dissolution (~0.078 Tg-Fe yr^{-1}) compared to the present day (~0.175 Tg-Fe yr^{-1}), while DFe biomass burning emissions are enhanced by 20% (~0.155 Tg-Fe yr^{-1} in the year 2100 against ~0.127 Tg-Fe yr^{-1} nowadays). Overall, the model calculates for 2100 a global DFe deposition of ~0.369 Tg-Fe yr^{-1} that is ~25% lower than the present day deposition.

Focusing on oceanic regions, an increase in DFe deposition of ~3 times is calculated for the last 150 years (0.063 Tg-Fe yr^{-1} in the year 1850 against ~0.191 Tg-Fe yr^{-1} nowadays) but a decrease of ~30% over HNLC oceans is projected for the future (0.024 Tg-Fe yr^{-1} in the year 2100 against ~0.033 Tg-Fe yr^{-1} nowadays). In view of the importance of Fe as a micronutrient for marine ecosystems, the calculated changes in Fe-containing aerosol solubility due to air-quality changes, indicate the necessity of the implementation of comprehensive mineral Fe-dissolution processes as well as Fe combustion emissions in

Deleted: 012

Deleted: 124

Deleted: an increase (~50%) in

Deleted: 230

Deleted: past

Deleted: 489

Deleted:

Deleted: also

Deleted: the future

Deleted: indicate that this will lead to reduced

Deleted: 076

Deleted: PRESENT one (~0.163 Tg-Fe yr^{-1}), as well as a lower

Deleted: (~

Deleted: 372

Deleted:).

Formatted: Space Before: 12 pt, Line spacing: 1.5 lines

Deleted: the HNLC waters

Deleted: 50%

Deleted: 20

Deleted: the Southern Ocean

Deleted: .

Deleted: the

Deleted: PAST, PRESENT and FUTURE

Deleted: dust

Deleted: in carbon-climate

coupled climate-biogeochemistry models to account for feedbacks between climate and biogeochemical cycles.

Deleted: by taking into account the air-quality changes in the global atmosphere

Acknowledgements

This research has been co-financed by the European Union (European Social Fund – ESF) and Greek national funds through the Operational Program "Education and Lifelong Learning" of the National Strategic Reference Framework (NSRF) - Research Funding Program: ARISTEIA – PANOPLY (Pollution Alters Natural Aerosol Composition: implications for Ocean Productivity, cLimate and air qualitY) grant. We would like to thank Dr. Z. Shi and Dr. S. Nickovic for fruitful discussions and the two anonymous reviewers for careful reading of the manuscript and useful comments.

Formatted: Font: 12 pt, Bold, Not Italic

Deleted: .

Formatted: Font: 12 pt

Formatted: Space Before: 12 pt, Line spacing: 1.5 lines

References

Baker, A. R., Adams, C., Bell, T. G., Jickells, T. D., and Ganzeveld, L.: Estimation of atmospheric nutrient inputs to the Atlantic Ocean from 50°N to 50°S based on large-scale field sampling: Iron and other dust-associated elements, Global Biogeochem. Cycles, 27, 755–767, doi:10.1002/gbc.20062, 2013.

Bonneville, S., Vancappellen, P. and Behrends, T.: Microbial reduction of iron(III) oxyhydroxides: effects of mineral solubility and availability, Chem. Geol., 212(3-4), 255–268, doi:10.1016/j.chemgeo.2004.08.015, 2004.

Boyd, P. W., Jickells, T., Law, C. S., Blain, S., Boyle, E. A., Buesseler, K. O., Coale, K. H., Cullen, J. J., de Baar, H. J. W., Follows, M., Harvey, M., Lancelot, C., Levasseur, M., Owens, N. P. J., Pollard, R., Rivkin, R. B., Sarmiento, J., Schoemann, V., Smetacek, V., Takeda, S., Tsuda, A., Turner, S., Watson A. J.: Mesoscale Iron Enrichment Experiments 1993–2005: Synthesis and Future Directions, Science, 315, 612, doi: 10.1126/science.1131669, 2007.

Boyd, P. W., Watson, A. J., Law, C. S., Abraham, E. R., Trull, T., Murdoch, R., Bakker, D. C., Bowie, A. R., Buesseler, K. O., Chang, H., Charette, M., Croot, P., Downing, K., Frew, R., Gall, M., Hadfield, M., Hall, J., Harvey, M., Jameson, G., LaRoche, J., Liddicoat, M., Ling, R., Maldonado, M. T., McKay, R. M., Nodder, S., Pickmere, S., Pridmore, R., Rintoul, S., Safi, K., Sutton, P., Strzepek, R., Tanneberger, K., Turner, S., Waite, A. and Zeldis, J.: A mesoscale phytoplankton bloom in the polar Southern Ocean stimulated by iron fertilization., Nature, 407(6805), 695–702, doi:10.1038/35037500, 2000.

Boyd, P.W., Strzepek R., Takeda S.,Wong, C. S. McKay, R.M.: The evolution and termination of an iron-induced mesoscale bloom in the northeast subarctic Pacific, Limnol. Oceanogr., 50(6), 1872–1886, 2005.

Carlton, A. G., Turpin, B. J., Altieri, K. E., Seitzinger, S., Reff, A., Lim, H.-J. and Ervens, B.: Atmospheric oxalic acid and SOA production from glyoxal: Results of aqueous photooxidation experiments, Atmos. Environ., 41(35), 7588–7602, doi:10.1016/j.atmosenv.2007.05.035, 2007.

Chen, H. and Grassian, V. H.: Iron dissolution of dust source materials during simulated acidic processing: the effect of sulfuric, acetic, and oxalic acids., Environ. Sci. Technol., 47(18), 10312–21, doi:10.1021/es401285s, 2013.

Daskalakis, N., Myriokefalitakis, S., and Kanakidou, M.: Sensitivity of tropospheric loads and lifetimes of short lived pollutants to fire emissions, Atmos. Chem. Phys., 15, 3543-3563, doi:10.5194/acp-15-3543-2015, 2015.

Dee, D. P., Uppala, S. M., Simmons, A. J., Berrisford, P., Poli, P., Kobayashi, S., Andrae, U., Balmaseda, M. A., Balsamo, G., Bauer, P., Bechtold, P., Beljaars, A. C. M., van de Berg, L., Bidlot, J., Bormann, N., Delsol, C., Dragani, R., Fuentes, M., Geer, A. J., Haimberger, L., Healy, S. B., Hersbach, H., Hólm, E. V., Isaksen, L., Kållberg, P., Köhler, M., Matricardi, M., McNally, A. P., Monge-Sanz, B. M., Morcrette, J. J., Park, B. K., Peubey, C., de Rosnay, P., Tavolato, C., Thépaut, J. N., and Vitart, F.: The ERA-Interim reanalysis: configuration and performance of the data assimilation system, Q. J. Roy. Meteor. Soc., 137, 553-597, doi: 10.1002/qj.828, 2011.

Deguillaume, L., Leriche, M., Monod, A. and Chaumerliac, N.: The role of transition metal ions on HO x radicals in clouds: a numerical evaluation of its impact on multiphase chemistry, Atmos. Chem. Phys., 4, 95-110, doi:10.5194/acp-4-95-2004, 2004.

Dentener, F., Kinne, S., Bond, T., Boucher, O.: Emissions of primary aerosol and precursor gases in the years 2000 and 1750 prescribed data-sets for AeroCom, Atmos. Chem. Phys., 6, 4321–4344, doi:10.5194/acp-6-4321-2006, 2006.

Duce, R., A. LaRoche, J., Altieri, K., Arrigo, K.R., Baker, A. R., Capone, D. G., Cornell, S.,Dentener, F., Galloway, J., Ganeshram, R. S., Geider, R. J., Jickells, T., Kuypers, M. M., Langlois, R., Liss, P. S., Liu, S. M., Middelburg, J. J., Moore, C. M., Nickovic, S., Oschlies, A., Pedersen, T., Prospero, J., Schlitzer, R., Seitzinger, S., Sorensen, L.

L., Uematsu, M., Ulloa, O., Voss, M., Ward, B., Zamora L.: Impacts of Atmospheric Anthropogenic Nitrogen on the Open Ocean, Science 320, 893, doi: 10.1126/science.1150369, 2008.

Ervens, B., George, C., Williams, J.E., Buxton, G.V., Salmon, G.A., Bydder, M., Wilkinson, F., Dentener, F., Mirabel, P., Wolke, R., Herrmann, H: CAPRAM 2.4 (MODAC mechanism): An extended and condensed tropospheric aqueous phase mechanism and its application, J. Geophys. Res., 108(D14), 1–21, doi:10.1029/2002JD002202, 2003.

Falkowski P., Scholes R.J., Boyle E., Canadell J., Canfield, D., Elser, J., Gruber, N., Hibbard, K., Högberg, P., Linder, S., Mackenzie, F. T., Moore III, B., Pedersen, T., Rosenthal, Y., Seitzinger, S., Smetacek, V., Steffen W.: The Global Carbon Cycle: A Test of Our Knowledge of Earth as a System, Science 290, 291,-296, doi: 10.1126/science.290.5490.291, 2000.

Fan, S.-M.: Impact of air pollution on wet deposition of mineral dust aerosols, Geophys. Res. Lett., 31(2), L02104, doi:10.1029/2003GL018501, 2004.

Formenti, P., Rajot, J. L., Desboeufs, K., Caquineau, S., Chevaillier, S., Nava, S., Gaudichet, A., Journet, E., Triquet, S., Alfaro, S., Chiari, M., Haywood, J., Coe, H., and Highwood, E.: Regional variability of the composition of mineral dust from western Africa: results from the AMMA SOP0/DABEX and DODO field campaigns, J. Geophys. Res., 113, D00C13, doi:10.1029/2008JD009903, 2008.

Formenti, P., Caquineau, S., Desboeufs, K., Klaver, A., Chevaillier, S., Journet, E., and Rajot, J. L.: Mapping the physico-chemical properties of mineral dust in western Africa: mineralogical composition, Atmos. Chem. Phys., 14, 10663–10686, doi:10.5194/acp-14-10663-2014, 2014.

Fountoukis, C. and Nenes, A.: ISORROPIA II: a computationally efficient thermodynamic equilibrium model for K^+–Ca^{2+}–Mg^{2+}–NH_4^+–Na^+–SO_4^{2-}–NO_3^-–Cl^-–

H_2O aerosols: Atmos. Chem. Phys., 7, 4639-4659, doi:10.5194/ acp-7-4639-2007, 2007.

Goudie, S.: Dust storms: Recent developments, J. Environ. Man., 90, 89–94, doi:10.1016/j.jenvman.2008.07.007, 2009.

Granier, C., Guenther, A., Lamarque, J., Mieville, A., Muller, J., Olivier, J., Orlando, J., Peters, J., Petron, G., Tyndall, G., and Wallens, S.: POET, a database of surface emissions of ozone pre- cursors, available at: http://www.pole-ether.fr/eccad (last access: December 2015), ECCAD-Ether Database, 2005.Granier, C., Guenther, A., Lamarque, J., Mieville, A., Muller, J., Olivier, J., Orlando, J., Peters, J., Petron, G., Tyndall, G., and Wallens, S.: POET, a database of surface emissions of ozone precursors, available at: http://www.aero.jussieu.fr/projet/ACCENT/POET.php, 2005.

Huneeus, N., Schulz, M., Balkanski, Y., Griesfeller, J., Prospero, J., Kinne, S., Bauer, S., Boucher, O., Chin, M., Dentener, F., Diehl, T., Easter, R., Fillmore, D., Ghan, S., Ginoux, P., Grini, A., Horowitz, L., Koch, D., Krol, M. C., Landing, W., Liu, X., Mahowald, N., Miller, R., Morcrette, J.-J., Myhre, G., Penner, J., Perlwitz, J., Stier, P., Takemura, T., and Zender, C. S.: Global dust model intercomparison in AeroCom phase I, Atmos. Chem. Phys., 11, 7781-7816, doi:10.5194/acp-11-7781-2011, 2011.

Ito, A. and Feng, Y.: Role of dust alkalinity in acid mobilization of iron, Atmos. Chem. Phys., 10, 9237-9250, doi:10.5194/acp-10-9237-2010, 2010.

Ito, A. and Xu, L.: Response of acid mobilization of iron-containing mineral dust to improvement of air quality projected in the future, Atmos. Chem. Phys., 14, 3441-3459, doi:10.5194/acp-14-3441-2014, 2014.

Ito, A.: Global modeling study of potentially bioavailable iron input from shipboard aerosol sources to the ocean, Global Biogeochem. Cycles, 27(1), 1–10, doi:10.1029/2012GB004378, 2013. Ito, A.: Global modeling study of potentially bioavailable iron input from shipboard aerosol sources to the ocean, Global Biogeochem. Cycles, 27, doi: 10.1029/2012GB004378, 2013.

Ito, A.: Atmospheric Processing of Combustion Aerosols as a Source of Bioavailable Iron, Environ. Sci. Technol. Lett., 2(3), 150203103108006, doi:10.1021/acs.estlett.5b00007, 2015.

Jeuken, A, Veefkind, J.P., Dentener, F., Metzger, S., Roble Gonzalez, C.: Simulation of the aerosol optical depth over Europe for August 1997 and a comparison with observations, J. Geophys. Res., 106, 28295-28311, 2001.

Jickells, T. D. and Spokes, L. J.: Atmospheric iron inputs to the oceans, in: The Biogeochemistry of Iron in Seawater, edited by: Turner, D. R. and Hunter, K., SCOR/IUPAC Series, John Wiley & Sons, New York, 410 pp., ISBN: 978-0-471-49068-5, 85–121, 2001.Jickells, T.D., Spokes, L.J.: Atmospheric iron inputs to the oceans, Turner, D.R., Hunter, K. (Eds.), The Biogeochemistry of Iron in Seawater, SCOR/IUPAC Series. J. Wiley, 85–121, 2001.

Johnson, M. S. and Meskhidze, N.: Atmospheric dissolved iron deposition to the global oceans: effects of oxalate-promoted Fe dissolution, photochemical redox cycling, and dust mineralogy, Geosci. Model Dev., 6, 1137-1155, doi:10.5194/gmd-6-1137-2013, 2014.

Johnson, M. S., Meskhidze, N., Solmon, F., Gasso, S., Chuang, P. Y., Gaiero, D. M., Yantosca, R. M., Wu, S., Wang, Y., and Carouge, C.: Modeling dust and soluble iron deposition to the South Atlantic Ocean, J. Geophys. Res., 115, D15202,doi:10.1029/2009JD013311, 2010.

Kalivitis N., E. Gerasopoulos, M. Vrekoussis., G. Kouvarakis, N. Kubilay, N. Hatzianastassiou., I. Vardavas, N. Mihalopoulos, Dust transport over the Eastern Mediterranean derived from TOMS, AERONET and surface measurements, J. Geophys. Res., 112 (D3): art. no. D03202, FEB 7 2007.

Koulouri, E., Saarikoski, S., Theodosi, C., Markaki, Z., Gerasopoulos, E., Kouvarakis, G., Mäkelä, T., Hillamo, R. and Mihalopoulos, N.: Chemical composition and sources of fine and coarse aerosol particles in the Eastern Mediterranean, Atmos. Environ., 42(26), 6542–6550, doi:10.1016/j.atmosenv.2008.04.010, 2008.

Kraemer, S. M.: Iron oxide dissolution and solubility in the presence of siderophores, Aquat. Sci. - Res. Across Boundaries, 66(1), 3–18, doi:10.1007/s00027-003-0690-5, 2004.

Lamarque, J.-F., Bond, T. C., Eyring, V., Granier, C., Heil, A., Klimont, Z., Lee, D., Liousse, C., Mieville, A., Owen, B., Schultz, M. G., Shindell, D., Smith, S. J., Stehfest, E., Van Aardenne, J., Cooper, O. R., Kainuma, M., Mahowald, N., McConnell, J. R., Naik, V., Riahi, K., and van Vuuren, D. P.: Historical (1850–2000) gridded anthropogenic and biomass burning emissions of reactive gases and aerosols: methodology and application, Atmos. Chem. Phys., 10, 7017-7039, doi:10.5194/acp-10-7017-2010, 2010.

Lamarque, J.-F., Shindell, D. T., Josse, B., Young, P. J., Cionni, I., Eyring, V., Bergmann, D., Cameron-Smith, P., Collins, W. J., Doherty, R., Dalsoren, S., Faluvegi, G., Folberth, G., Ghan, S. J., Horowitz, L. W., Lee, Y. H., MacKenzie, I. A., Nagashima, T., Naik, V., Plummer, D., Righi, M., Rumbold, S. T., Schulz, M., Skeie, R. B., Stevenson, D. S., Strode, S., Sudo, K., Szopa, S., Voulgarakis, A. and Zeng, G.: The Atmospheric Chemistry and Climate Model Intercomparison Project (ACCMIP): overview and description of models, simulations and climate diagnostics, Geosci. Model Dev., 6(1), 179–206, doi:10.5194/gmd-6-179-2013, 2013..

Lanzl, C. A., Baltrusaitis, J. and Cwiertny, D. M.: Dissolution of hematite nanoparticle aggregates: influence of primary particle size, dissolution mechanism, and solution pH., Langmuir, 28(45), 15797–808, doi:10.1021/la3022497, 2012.

Lasaga, A. C., Soler, J. M., Ganor, J., Burch, T. E., and Nagy, K. L.: Chemical-weathering rate laws and global geochemical cycles, Geochim. Cosmochim. Ac., 58, 2361–2386, 1994.

Lim, Y. B., Tan, Y., and Turpin, B. J.: Chemical insights, explicit chemistry, and yields of secondary organic aerosol from OH radical oxidation of methylglyoxal and glyoxal in the aqueous phase, Atmos. Chem. Phys., 13, 8651-8667, doi:10.5194/acp-13-8651-2013, 2013.

Lim, Y.B., Tan Y., Perri, M.J., Seitzinger, S. P., and Turpin, B.J.: Aqueous chemistry and its role in secondary organic aerosol (SOA) formation, Atmos. Chem. Phys., 10, 10521–10539, doi:10.5194/acp-10-10521-2010, 2010.

Lin, G., Sillman, S., Penner, J. E. and Ito, A.: Global modeling of SOA: The use of different mechanisms for aqueous-phase formation, Atmos. Chem. Phys., 14, 5451–5475, doi:10.5194/acp-14-5451-2014, 2014.

Louis, J. – F., A parametric model of vertical eddy fluxes in the atmosphere, Bound. Layer Meteorol., 17, 187 – 202, 1979.

Luo, C., Mahowald N., Bond, T., Chuang, P. Y., Artaxo, P. Siefert, R., Chen, Y., Schauer, J.: Combustion iron distribution and deposition, Global Biogeochem. Cycles, 22, doi:10.1029/2007GB002964, 2008.

Luo, C., N. M. Mahowald, N. Meskhidze, Y. Chen, R. L. Siefert, A. R. Baker, and Johansen A. M.: Estimation of iron solubility from observations and a global aerosol model, J. Geophys. Res., 110, D23307, doi:10.1029/2005JD006059, 2005.

Luo, C., N. Mahowald, T. Bond, P. Y. Chuang, P. Artaxo, R. Siefert, Y. Chen, and Schauer J.: Combustion iron distribution and deposition, Global Biogeochem. Cycles, 22, GB1012, doi:10.1029/2007GB002964, 2008.

Maher, B.A., Prospero, J.M. Mackie, D., Gaiero, D., Hesse, P.P., Balkanski, Y.: Global connections between aeolian dust, climate and ocean biogeochemistry at the present day and at the last glacial maximum, Earth-Science Reviews 99 61–97, doi:10.1016/j.earscirev.2009.12.001, 2010.

Mahowald, N. M., Baker, A. R., Bergametti, G., Brooks, N., Duce, R. A., Jickells T. D., Kubilay N., Prospero, J. M., Tegen, Ina: The atmospheric global dust cycle and iron inputs to the ocean, Global Biogeochem. Cycles, 19, GB4025, doi:10.1029/2004GB002402, 2005.

Mahowald, N., Engelstaedter, S., Luo, C., Sealy, A., Artaxo, P., Benitez-Nelson, C., Bonnet, S., Chen, Y., Chuang, P. Y., Cohen, D. D., Dulac, F., Herut, B., Johansen, A. M., Kubilay, N., Losno, R., Maenhaut, W., Paytan, A., Prospero, J. M., Shank, L. M., and Siefert, R. L.: Atmospheric Iron deposition: Global distribution, variability and human perturbations, Annu. Rev. Mar. Sci., 1, 245–278, doi:210.1146/annurev/marine.010908.163727, 2009.

Mahowald, N.M., Baker, A.R., Bergametti, G., Brooks, N., Duce, R.A., Jickells, T.D., Kubilay, N., Prospero, J.M. and Tegen, I.: Atmospheric global dust cycle and iron inputs to the ocean, Global Biogeochem. Cycles, 19, GB4025, doi:10.1029/2004GB002402, 2005.

Martin, J.H., and Fitzwater S.E.: Iron deficiency limits phytoplankton growth in the north-east Pacific subarctic, Nature 331, 341 – 343, doi:10.1038/331341a0, 1988.

McNeill, V.F., Woo, J.L.. Kim, D.D., Schwier, A.N., Wannell, N.J., Sumner, A.J., and Barakat J.M.: Aqueous-Phase Secondary Organic Aerosol and Organosulfate Formation in Atmospheric Aerosols: A Modeling Study, Environ. Sci. Technol., 46, 8075−8081dx.doi.org/10.1021/es3002986, 2012.

Meskhidze N., Chameides W.L. and Nenes A.: Dust and pollution: A recipe for enhanced ocean fertilization?, J. Geophys. Res., 110, d03301, doi:10.1029/2004jd005082, 2005.

Moore, J. K. and Doney, S. C.: Iron availability limits the ocean nitrogen inventory stabilizing feedbacks between marine denitrification and nitrogen fixation, Global Biogeochem. Cycles, 21(2), n/a–n/a, doi:10.1029/2006GB002762, 2007.

Myriokefalitakis, S., Tsigaridis, K., Mihalopoulos, N., Sciare, J., Nenes, A., Kawamura, K., Segers, A., and Kanakidou, M.: In-cloud oxalate formation in the global troposphere: a 3-D modeling study, Atmos. Chem. Phys., 11, 5761–5782, doi:10.5194/acp-11-5761-2011, 2011.

Myriokefalitakis, S., Vignati, E., Tsigaridis, K., Papadimas, C., Sciare J., Mihalopoulos, N., Facchini, M.C., Rinaldi, M., Dentener, F.J., Ceburnis, D., Hatzianastasiou, N., O'Dowd, C.D., van Weele, M., Kanakidou, M.: Global modelling of the oceanic source of organic aerosols, Adv. Meteorol., 2010, 939171, 16 pp., doi:10.1155/2010/939171, 2010.

Myriokefalitakis, S., Vrekoussis, M., Tsigaridis, K., Wittrock, F., Richter, A., Bruhl, C., Volkamer, R., Burrows, J. P., and Kanakidou, M.: The influence of natural and anthropogenic secondary sources on the glyoxal global distribution, Atmos. Chem. Phys., 8, 4965–4981, doi:10.5194/acp-8-4965-2008, 2008.

Nenes, A., Krom, M. D., Mihalopoulos, N., Van Cappellen, P., Shi, Z., Bougiatioti, A., Zarmpas, P., and Herut, B.: Atmospheric acidification of mineral aerosols: a source of bioavailable phosphorus for the oceans, Atmos. Chem. Phys., 11, 6265-6272, doi:10.5194/acp-11-6265-2011, 2011.

Nickovic, S., Vukovic, A., and Vujadinovic, M. (2013) Atmospheric processing of iron carried by mineral dust, Atmos. Chem. Phys., 13, 9169-9181, doi:10.5194/acp-13-9169-2013.

Nickovic, S., Vukovic, A., Vujadinovic, M., Djurdjevic, V., and Pejanovic, G.: Technical Note: High-resolution mineralogical database of dust-productive soils for atmospheric dust modeling, Atmos. Chem. Phys., 12, 845-855, doi:10.5194/acp-12-845-2012, 2012.

Oakes, M., Ingall, E. D., Lai, B., Shafer, M. M., Hays, M. D., Liu, Z. G., Russell, A. G., and Weber, R. J.: Iron solubility related to particle sulfur content in source emission and ambient fine particles, Environ. Sci. Technol., 46, 6637–6644, 2012.

Okin, G. S., Baker, A. R., Tegen, I., Mahowald, N. M., Dentener, F. J., Duce, R. A., Galloway, J. N., Hunter, K., Kanakidou, M., Kubilay, N., Prospero, J. M., Sarin, M., Surapipith, V., Uematsu, M. and Zhu, T.: Impacts of atmospheric nutrient deposition on marine productivity: Roles of nitrogen, phosphorus, and iron, Global Biogeochem. Cycles, 25(2), GB2022, doi:10.1029/2010GB003858, 2011.

Olivie, D. J. L., van Velthoven, P. F. J., Beljaars, A. C. M., and Kelder H. M.: Comparison between archived and off – line diagnosed convective mass fluxes in the chemistry transport model TM3, J. Geophys. Res., 109, D11303, doi:10.1029/2003JD004036, 2004.

Paris, R. and Desboeufs, K. V.: Effect of atmospheric organic complexation on iron-bearing dust solubility, Atmos. Chem. Phys., 13, 4895-4905, doi:10.5194/acp-13-4895-2013, 2013.

Paris, R., Desboeufs, K. and Journet, E.: Variability of dust iron solubility in atmospheric waters: Investigation of the role of oxalate organic complexation, Atmos. Environ., 45(36), 6510–6517, doi:10.1016/j.atmosenv.2011.08.068, 2011. Paris R.K., Desboeufs V., Journe E.: Variability of dust iron solubility in atmospheric waters: Investigation of the role of oxalate organic complexation, Atmos. Environ., 45, doi:10.1016/j.atmosenv.2011.08.068, 2011.

Raes, F., Van Dingenen, R., Vignati, E., Wilson, J., Putaud, J.-P., Seinfeld, J. H., Adams, P.: Formation and cycling of aerosols in the global troposphere, Atmos. Environ., 34, 4215-4240, 2000.

Russell, G. L. and Lerner, J. a.: A New Finite-Differencing Scheme for the Tracer Transport Equation, J. Appl. Meteorol., 20, 1483–1498, doi:10.1175/1520-0450(1981)020<1483:ANFDSF>2.0.CO;2, 1981.

Seinfeld, J. H. and Pandis, S. N.: Atmospheric Chemistry and Physics: From Air Pollution to Climate Change, A Wiley Interscience publication, New York, USA, 1998.

Shao, Y., Wyrwoll, K.-H., Chappell, A., Huang, J., Zhaohui, L., McTainsh G.H., Mikami, M., Tanaka, T. Y., Wang, X., Yoon, S.: Dust cycle: An emerging core theme in Earth system science, Aeol. Res. 2, 181–204, doi:10.1016/j.aeolia.2011.02.00, 2011.

Shi, Z., Bonneville, S., Krom, M. D., Carslaw, K. S., Jickells, T. D., Baker, A. R., and Benning, L. G.: Iron dissolution kinetics of mineral dust at low pH during simulated atmospheric processing, Atmos. Chem. Phys., 11, 995-1007, doi:10.5194/acp-11-995-2011, 2011a.

Shi, Z., Krom M., Bonneville, S., Baker, A.R., Bristow, C., Drake, N., Mann, G., Carslaw, K., McQuaid, J.B., Jickells, T., and Benning, L.G.: Influence of chemical weathering and aging of iron oxides on the potential iron solubility of Saharan dust during simulated atmospheric processing, Global Biogeochem. Cycles, 25, GB2010, doi:10.1029/2010GB003837, 2011b.

Shi, Z., Krom, M.D., Jickells T.D., Bonneville, S., Carslaw, K.S., Mihalopoulos, N., Baker, A.R., Benning, L.G.: Impacts on iron solubility in the mineral dust by processes in the source region and the atmosphere: A review, Aeol. Res. 5, 21–42, http://dx.doi.org/10.1016/j.aeolia.2012.03.001, 2012.

Sholkovitz E. R., Sedwick P. N., Church T. M., Baker A. R., and Powell C. F.: Fractional solubility of aerosol iron: synthesis of a global-scale data set, Geochim. Cosmochim. Acta, 89, 173–189 doi:10.1016/j.gca.2012.04.022, 2012.

Sindelarova, K., Granier, C., Bouarar, I., Guenther, A., Tilmes, S., Stavrakou, T., Müller, J.-F., Kuhn, U., Stefani, P., and Knorr, W.: Global data set of biogenic VOC emissions calculated by the MEGAN model over the last 30 years, Atmos. Chem. Phys., 14, 9317–9341, doi:10.5194/acp-14-9317-2014, 2014.Sindelarova, K., Granier, C., Bouarar, I., Guenther, A., Tilmes, S., Stavrakou, T., Müller, J.-F., Kuhn, U., Stefani, P., and Knorr, W.: Global dataset of biogenic VOC emissions calculated by the MEGAN model over the last 30 years, Atmos. Chem. Phys. Discuss., 14, 10725-10788, doi:10.5194/acpd-14-10725-2014, 2014.

Solmon, F., Chuang, P. Y., Meskhidze, N., and Chen, Y.: Acidic processing of mineral dust iron by anthropogenic compounds over the north Pacific Ocean, J. Geophys. Res., 114, D02305, doi:10.1029/2008JD010417, 2009.

Stumm, W. and Morgan, J. J.: Aquatic Chemistry, 3rd edn., J. Wiley-Interscience, New York, 1022 pp., 1996.

Stumm, W. and Sulzberger, B.: The cycling of iron in natural environments: Considerations based on laboratory studies of heterogeneous redox processes, Geochim. Cosmochim. Ac., 56, 3233–3257, 1992.

Taylor, S.R., and McLennan S.M.: The Continental Crust: Its Composition and Evolution, 312 pp., Blackwell, Malden, Mass., 1985.

Theodosi C., Markaki, Z., Mihalopoulos N.: Iron speciation, solubility and temporal variability in wet and dry deposition in the Eastern Mediterranean, Mar. Chem., 120, 100–107, doi:10.1016/j.marchem.2008.05.004, 2010.

Theodosi C., Markaki, Z., Tselepidis, A., Mihalopoulos N.: The significance of atmospheric inputs of soluble and particulate major and trace metals to the eastern Mediterranean seawater, Marine Chemistry, 120, 154–163, 2010.

Tiedke, M., A comprehensive mass flux scheme for cumulus parameterization in large – scale models, Mon. Weather Rev., 117, 1779 –1800, 1989.

Tsigaridis K., and M., Kanakidou, Secondary organic aerosol importance in the future atmosphere, Atmos. Environ, 41, 4682–4692, doi:10.1016/j.atmosenv.2007.03.045, 2007.

Tsigaridis K., Kanakidou M, Global modelling of secondary organic aerosol in the troposphere: A sensitivity analysis, Atmos. Chem. Phys., 3, 1849-1869, 2003.

Tsigaridis, K., Krol, M., Dentener, F. J., Balkanski, Y., Lathi` ere, J., Metzger, S., Hauglustaine, D. A., and Kanakidou, M.: Change in global aerosol composition since preindustrial times, Atmos. Chem. Phys., 6, 5143–5162, doi:10.5194/acp-6-5143-2006, 2006.

Van Noije, T. P. C., Eskes, H. J., van Weele, M. and van Velthoven, P. F. J.: Implications of the enhanced Brewer-Dobson circulation in European Centre for Medium-Range Weather Forecasts reanalysis ERA-40 for the stratosphere-troposphere exchange of ozone in global chemistry transport models, J. Geophys. Res. D Atmos., 109, 1–13, doi:10.1029/2004JD004586, 2004.

Witt, M., Baker, A. R., and Jickells T. D.: Atmospheric trace metals over the Atlantic and South Indian Oceans: Investigation of metal concentrations and lead isotope ratios in coastal and remote marine aerosols, Atm. Environ., 40, 5435-5451, doi: 10.1016/j.atmosenv.2006.04.041, 2006.

Zhu, X.R., Prospero, J.M., Millero, F.J., Savoie, D.L.: The photochemical reaction in marine aerosol solution and its impact to iron concentration. J. Geophys. Res. 98, 9039–9047, 1993.

Tables

Table 1. Emissions of dust (in Tg yr^{-1}), Fe contained in dust-minerals (illite, kaolinite, smectite, hematite and feldspars; in Tg-Fe yr^{-1}), TFe and DFe (in Tg-Fe yr^{-1}) used in TM4-ECPL for a) present (year 2008), b) past (year 1850) and c) future (year 2100) simulations.

Species	**Year**	**Biomass Burning**	**Anthropogenic Combustion**	**Ships' Oil Combustion**	**Soils**
Dust	2008				1091
Fe (illite)	2008				8.473
Fe (kaolinite)	2008				0.871
Fe (smectite)	2008				17.154
Fe (hematite[*])	2008				5.663
Fe (feldspars)	2008				2.761
TFe	1850	0.120	0.147	9.83E-05	35.048
	2008	1.200	0.768	0.015	
	2100	1.456	0.158	0.002	
DFe	1850	0.013	0.011	7.99E-05	0.125
	2008	0.127	0.058	0.012	
	2100	0.155	0.012	0.001	

[*] *Hematite is here used as surrogate for Hematite and Goethite*

Deleted: Ships
Deleted: DUST
Deleted: 1090
Deleted: ILLITE
Deleted: 7.860
Deleted: KAOLINITE
Deleted: 921
Deleted: SMECTITE
Deleted: 16.100
Deleted: HEMATITE
Deleted: 690
Deleted: FELDSPAR
Deleted: 800
Deleted: 107
Deleted: 136
Deleted: 33.400
Deleted: 070
Deleted: 697
Deleted: 300
Deleted: 144
Deleted: 059
Deleted: 128
Deleted: 154
Deleted: ¶
¶

Table 2. Constants used for proton-promoted iron dissolution rates and emissions calculations for different types of iron-containing minerals: Water soluble/Dissolved iron (DFe); Fast-released iron (Fe_F); Intermediate-released iron (Fe_I); Slowly-released iron (Fe_S); Refractory iron (Fe_R). The parentheses contain the percentage content of Fe type in each mineral.

Mineral	Fe type	K_{MIN} (mol m^{-2} s^{-1})	m	A_{MIN} (m^2 g^{-1})	K_{eq}	n
Illite	Fe_F (2.7%) $^{(a}$	1.17x10^{-09}exp[9.2x10^{3}(1/298-1/T)] $^{(b}$	1$^{(b,c}$	205$^{(b,e}$	41.7	2.75
	Fe_S (97.3%)	1.30x10^{-11}exp[6.7x10^{3}(1/298-1/T)] $^{(d}$	0.39 $^{(d}$	90 $^{(d}$		
Smectite	Fe_I (5%) $^{(a}$	8.78x10^{-10}exp[9.2x10^{3}(1/298-1/T)] $^{(b}$	1$^{(b,c}$	125$^{(b,e}$	3.31	2.85
	Fe_S (95%)	8.10x10^{-12}exp[6.7x10^{3}(1/298-1/T)] $^{(d}$	0.3$^{(d}$	300 $^{(d}$		
Hematite*	Fe_R (100%) $^{(b}$	1.80x10^{-11}exp[9.2x10^{3}(1/298-1/T)] $^{(b}$	0.5$^{(e}$	9 $^{(b,a}$	0.44	2.85
Kaolinite	DFe(4.3%) $^{(b}$					
	Fe_R (95.7%)	4.00x10^{-11}exp[6.7x10^{3}(1/298-1/T)] $^{(f}$	0.1$^{(f}$	20 $^{(f}$	0.44$^{(b}$	2.85$^{(b}$
Feldspars	DFe (3%) $^{(b}$					
	Fe_R (97%)	2.4x10^{-10}exp[7.7x10^{3}(1/298-1/T)] $^{(f}$	0.5$^{(f}$	1$^{(f}$	0.44$^{(b}$	2.85$^{(b}$

a) Shi et al, 2011b; b) Ito and Xu, 2014; c) Lanzl et al., 2012; d) Ito, 2012; e) Bonneville et al., 2004; f) Meskhidze et al., 2005 and references therein.

**Hematite is here used as surrogate for Hematite and Goethite*

Deleted: Iron

Deleted: Iron

Deleted: Iron

Deleted: Iron

Deleted: Iron

Deleted: ILLITE

Deleted: SMECTITE

Deleted: HEMATITE

Deleted: KAOLINITE

Formatted: Font: 11 pt, Bold

Deleted: 1.80x10

Deleted: 9.2x10^{3}

Deleted: FELDSPARS

Deleted: 1.80x10^{-11}exp[9.2x10^{3}

Deleted: *Bonnevile*

Formatted: French (France)

Deleted: .¶
Table 3 Constants used for ligand (oxalate)-promoted iron mobilisation from Illite

Formatted: English (United States)

Deleted: Hematite.

Deleted: (see text).

Table 3. Constants used for ligand (oxalate)-promoted iron dissolution from illite and hematite.

Mineral	Dissolution rates (mol Fe m^{-2} s^{-1})	A_{min} (m^2 g^{-1})	Ref.
Illite	3.00×10^{-10} [OXL^{2-}] + 6×10^{-11}	205	Paris et al., 2011; Johnson and Meskhidze, 2013
Hematite[*]	0.36 *(3.00×10^{-12} [OXL^{2-}] – 2×10^{-12}) + 0.64*(1.00×10^{-11} [OXL^{2-}] + 7×10^{-13})	9	Paris et al., 2011; Johnson and Meskhidze, 2013

[*] *Hematite is here used as surrogate for Hematite and Goethite*

Deleted: References

Deleted: ILLITE

Deleted: HEMATITE

Figures

Figure 1. Atmospheric processing of dust-Fe taken into account in the model. Details on the chemical reactions are given in Table S2.

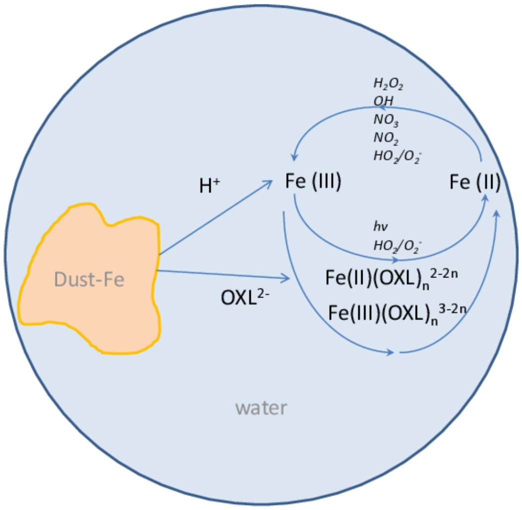

Figure 2. Annual averaged distributions (in ng-Fe m^{-2} s^{-1}) of a) total anthropogenic DFe primary emissions, b) total biomass burning DFe emissions, c) total DFe mineral emissions and d) total mineral-Fe dissolution flux as calculated by TM4-ECPL for the present atmosphere.

Deleted: (2008)

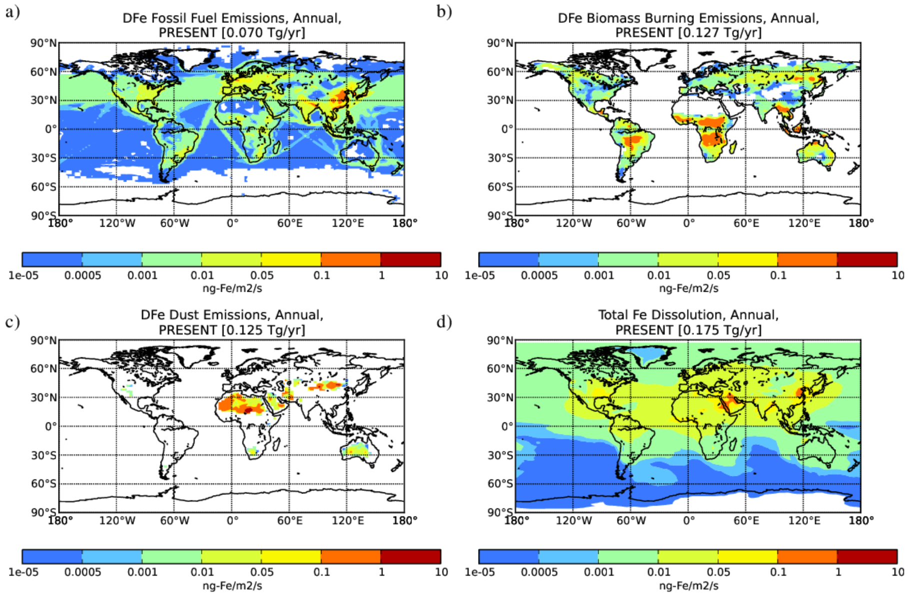

Figure 3. Annual averaged a) proton-promoted and b) ligand-promoted mineral-Fe dissolution flux (in ng-Fe m^{-2} s^{-1}) as calculated by TM4-ECPL for the present atmosphere.

Deleted: (2008)

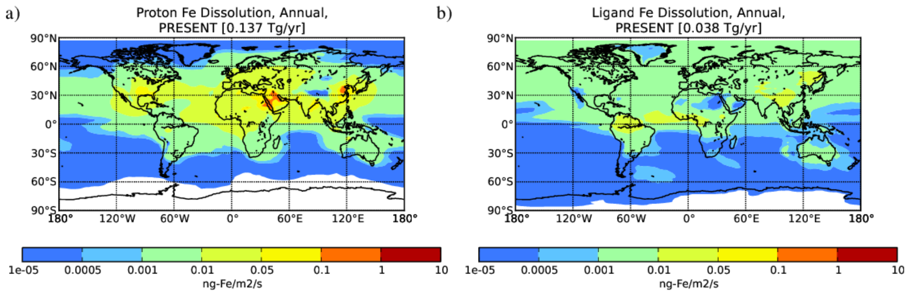

Figure 4. Calculated annual mean surface concentrations for the present atmosphere for (a) TFe in μg-Fe m^{-3}; (b) DFe in ng-Fe m^{-3} (c); and the percent fraction of Fe(II) to total DFe (%Fe(II)/DFe).

Deleted: %

Deleted: fraction

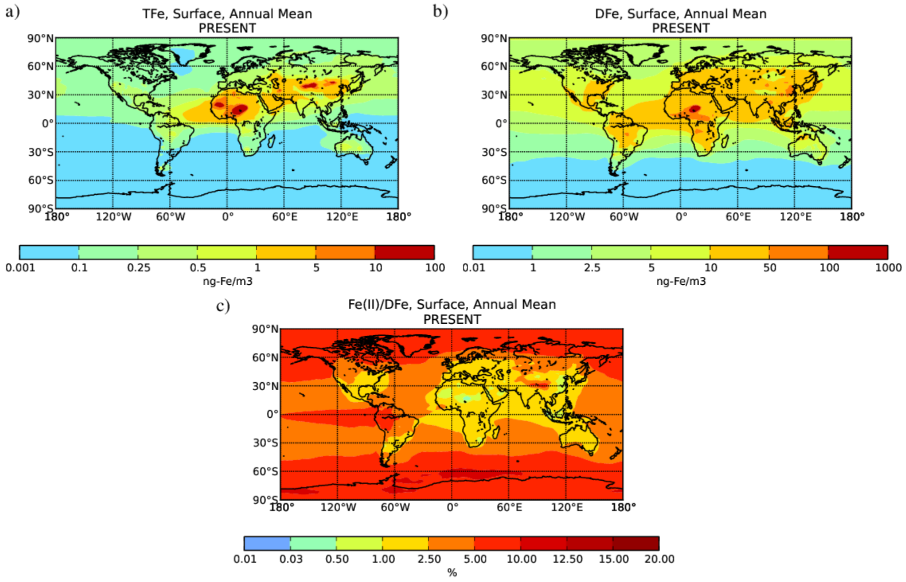

Figure 5. Log-scatter plot of model (y-axis) comparison with cruises observations over the Atlantic Ocean (Baker et al., 2013) and Indian Ocean (Witt et al., 2006) (x-axis) for a) TFe, b) the DFe and c) the SFe fractions in ambient aerosols, d) TFe comparison with global observations from Mahowland et al. (2005) and e) timeseries of monthly variation of TFe in ambient aerosols at Finokalia station (Koulouri et al., 2008); monthly mean observations are marked with dots, their variability is shown with the dashed are, model results are plotted by the black continuous line. In the scatter plots, the continuous black line shows the 1:1 correlation, while the dashed lines show the 10:1 and 1:10 relationships.

Deleted: Scatter

Deleted: and

Deleted: fraction

Deleted: c) log-Scatter plot of model (y-axis)

Deleted: d

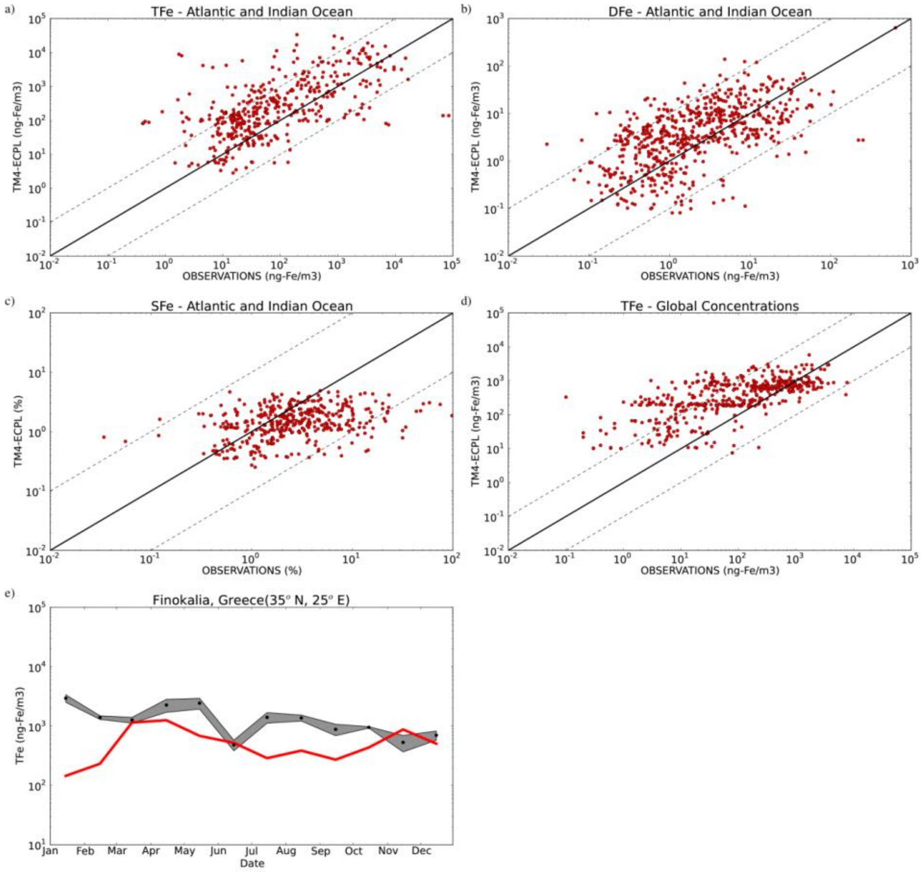

Figure 6. Calculated present annual deposition (in ng-Fe m^{-2} s^{-1}) for a) TFe, b) DFe, and the seasonal DFe deposition fluxes for c) December, January and February (DJF); d) March, April and May (MAM); e) June, July and August (JJA) and f) September, October and November (SON). In brackets (parentheses) the amounts of Fe deposition over the globe (only over oceans) are provided.

Deleted: shown

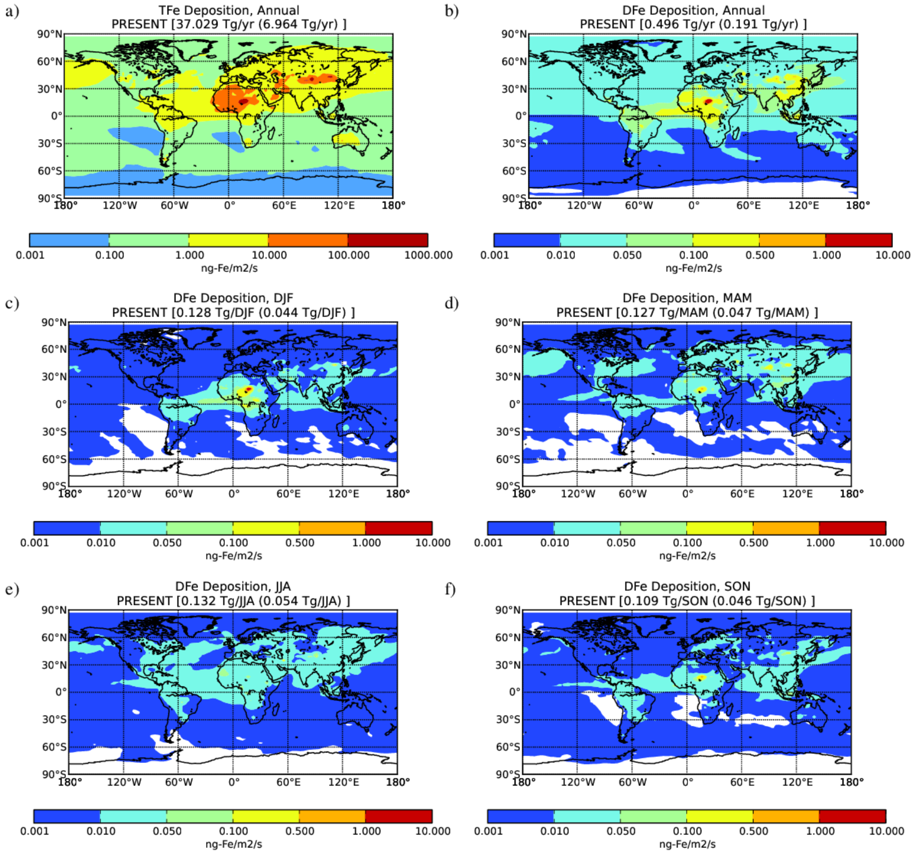

Figure 7. Comparison of Total Fe (TFe) and Dissolved Fe (DFe) input estimates to four Atlantic Ocean regions during the April-May-June (AMJ) and September-October-November (SON) periods (in Gmol-Fe) as compiled by Baker et al. (2013).

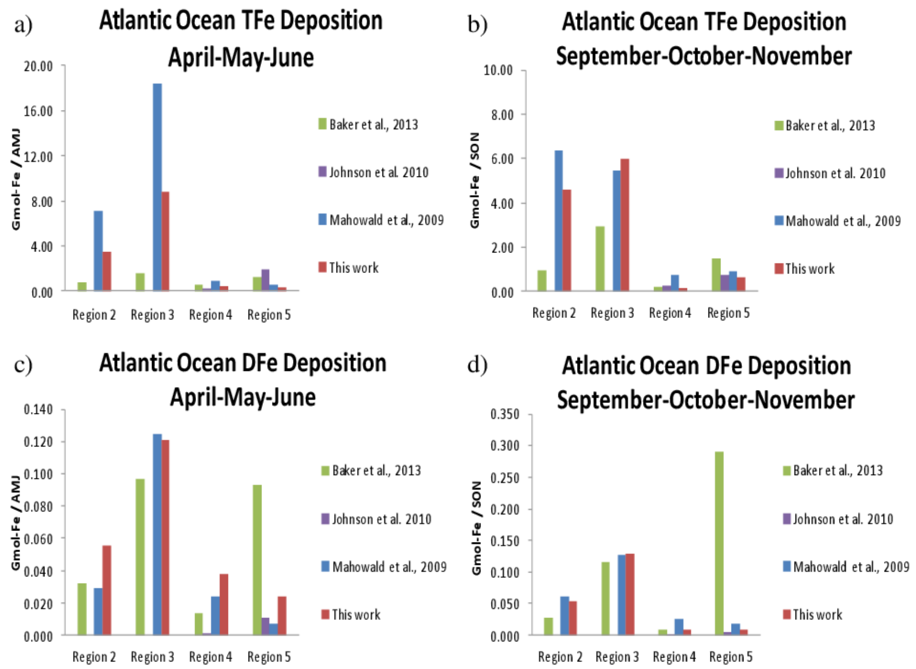

Figure 8. The percentage differences of PAST (left panels: a, c, e) and FUTURE (right panels: b, d, f) simulations from the PRESENT simulation for a, b) Proton-promoted/Total mineral-Fe Dissolution Fraction and c, d) Ligand-promoted/Total mineral-Fe Dissolution Fraction.

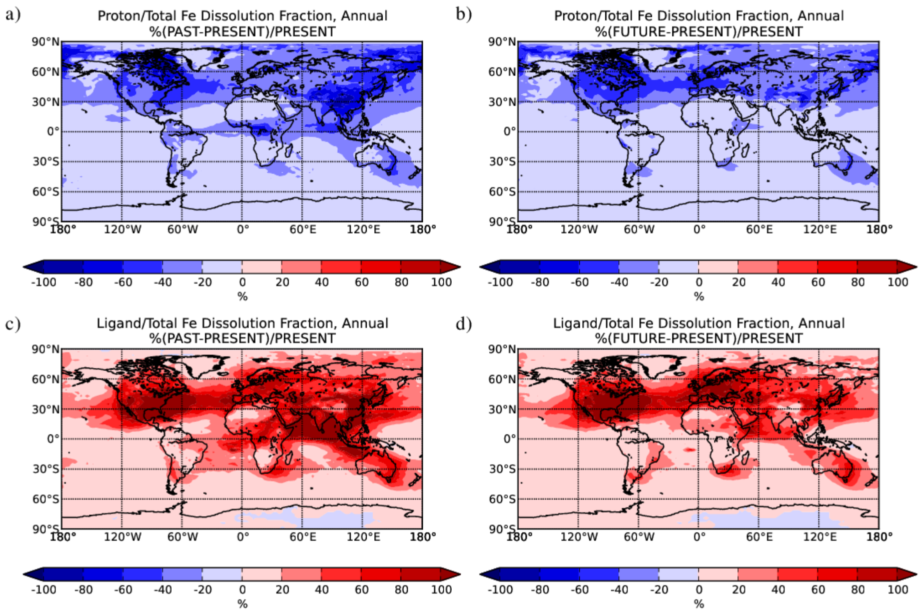

Figure 9. Calculated present annual deposition over oceans (in ng-Fe m^{-2} s^{-1}; in brackets (parentheses) the amounts of Fe deposition over oceans (only over HNLC regions are provided)) for a) TFe and b) DFe ; and the percentage (%) differences in DFe deposition of c) PAST and d) FUTURE simulations from the PRESENT simulation.

Deleted: Present

Deleted:) over

Deleted: (%)